





Soft-In Soft-Out Polar Decoding Aided Three-Stage Concatenated Iterative MIMO-Turbo Transceivers

ZEYNEP B. KAYKAC EGILMEZ  (Member, IEEE), **ROBERT G. MAUNDER**  (Senior Member, IEEE),
MOHAMMED EL-HAJJAR  (Senior Member, IEEE), AND **LAJOS HANZO**  (Life Fellow, IEEE)

School of Electronics and Computer Science, University of Southampton, SO17 1BJ Southampton, U.K.

CORRESPONDING AUTHOR: LAJOS HANZO (e-mail: lh@ecs.soton.ac.uk).

The work of Lajos Hanzo was supported in part by the Engineering and Physical Sciences Research Council under Grants EP/W016605/1, EP/X01228X/1, and EP/Y026721/1, and in part by the European Research Council's Advanced Fellow Grant QuantCom under Grant 789028.

ABSTRACT A novel Soft-Input Soft-Output (SISO) polar decoding algorithm is proposed, which is capable of iterating between an inner and outer decoder in a three-stage serial concatenated iterative receiver. The proposed polar decoding algorithm leverages a hybrid of Soft Cancellation (SCAN) and g -function aided-SCAN (G-SCAN) decoding. The SCAN decoder enables iterative soft-information exchange with the outer decoders and the G-SCAN decoder facilitates iterative soft-information exchange with the inner decoders while exploiting the error correction capability of the classic Successive Cancellation List (SCL) decoder. Furthermore, we present the Three-Dimensional (3D) Extrinsic Information Transfer (EXIT) chart analysis of polar codes for the first time, in order to characterise the iterative exchange of extrinsic information between these three concatenated stages. This offers an insight into the interactions of these three decoders and characterises their iterative convergence. In this three-stage serial concatenated scheme the first stage is a Joint Source Channel Coding (JSCC) decoder, the second stage is a 5th Generation (5G) 3rd Generation Partnership Project (3GPP) New Radio (NR) polar decoder based on our novel hybrid SISO polar algorithm, and the third stage is a 2×2 Multiple Input Multiple Output (MIMO) detector. We characterized the Symbol Error Rate (SER) vs. complexity of the proposed scheme, and compare it to various soft- and hard-decision benchmarks, as well as to the relevant JSCC and Separate Source Channel Coding (SSCC) schemes. In comparison to a three-stage serial concatenated JSCC benchmark, the proposed SISO scheme offers 11% complexity reduction over to the state-of-the-art SISO SCAN polar decoder at a similar SER performance. Additionally, the proposed SISO scheme achieves a 0.75 dB SNR gain over the SCAN polar decoder of a two-stage serial concatenated SSCC benchmark.

INDEX TERMS Turbo detection, MIMO detection, EXIT chart, soft-in soft-out, iterative polar decoding, 5G, NR.

I. INTRODUCTION

Recently, the 3rd Generation Partnership Project's (3GPP) 5th Generation (5G) New Radio (NR) standard has adopted Low-Density Parity-Check (LDPC) codes for data channels and polar codes for control channels [1]. Although polar codes were chosen for their superior error correction capabilities at short information block lengths only for the control channels, they have potential in many applications beyond control channels. Their strong performance makes them a promising

option for different applications including joint iterative detection and decoding (JIDD) schemes [2], [3], [4], [5], [6], as well as joint source and channel coding (JSCC) schemes [7], [8], [9].

Following the standardization of polar codes in the 3GPP 5G NR [1], a number of advanced polar decoding algorithms have been proposed [10], [11], [12], [13], [14]. Although the state-of-the-art Successive Cancellation List (SCL) [11] decoder has been shown to offer the best error correction

TABLE 1. Contrasting Our Contribution With the State-of-The-Art SISO Polar Decoders, as Well as With Existing Literature

Contributions	This work	[25]	[22]	BP [14]	SCAN [12]	BPL [26]	CA-BPL [27]	G-SCAN [21]
Soft information outputs	✓	✓	✓	✓	✓	✓	✓	✓
Propose SISO polar decoding algorithm	✓			✓	✓	✓	✓	✓
Turbo-detection applications	✓	✓	✓					✓
5G NR polar code applications	✓					✓	✓	✓
A JSCC is serially concatenated with a SISO channel decoder	with Polar codes	with LDPC	with Turbo codes					
Serial concatenation with an UEC JSCC code	✓		✓					
Serial concatenation with a MIMO detector	✓							✓
Three-stage serial concatenation of polar decoding	✓							
3D EXIT chart analysis	✓							

performance, it only produces hard-decision outputs, which prevents achieving iterative gains in iterative decoders [15], [16], [17], [18]. This has motivated the design of several soft-output polar decoders including the Soft Cancellation (SCAN) [12] algorithm. It has been shown that the SCAN polar decoder allows the iterative exchange of extrinsic information with an inner decoder, enabling joint decoding and detection for polar codes concatenated with an inner component such as a Multiple Input Multiple Output (MIMO)-detector [18], [19], [20]. However, our previous work [21] showed that even when iterating with an inner detector, the SCAN decoder may not perform better than the SCL decoder, which is incapable of exchanging extrinsic information with a MIMO detector and hence can only benefit from 'one-shot' MIMO detection. Motivated by this, our previous work [21] introduced a novel soft-in and soft-out G-SCAN polar decoder which is particularly suitable for iterations with an inner decoder. This offers the best of both worlds by simultaneously generating soft outputs for attaining iterative gains, as well as hard outputs that can improve upon the SCL performance.

However, Soft-Input Soft-Output (SISO) polar decoders have not been characterised in the context of three-stage schemes in concatenation with both an inner and an outer decoder. Such a polar decoder would have to accept *a-priori* information pertaining to both the encoded as well as decoded bits, and produce extrinsic information pertaining to both bit sequences in return. This would then allow an iterative exchange of extrinsic information with a concatenated inner component, such as a MIMO detector [15], [16], [17], [18], as well as a concatenated outer JSCC decoder [22], [23]. Motivated by this, the application of SISO polar decoders to a three-stage serial concatenated scheme is introduced in this article, where we propose a novel hybrid polar decoder that behaves as a SCAN decoder upon iterating with an outer code, and behaves as a G-SCAN decoder, where iterating with an inner detector. Against this background, we boldly and

explicitly contrast our contributions to the recently published literature in Table 1. In detail, the novel contributions of this article are summarised as follows:

- For the first time, we demonstrate the three-stage serial concatenation of a polar decoder, which iteratively exchanges extrinsic soft information both with an inner and an outer decoder. More specifically, a novel SISO hybrid polar decoding algorithm is proposed, which is capable of exchanging extrinsic soft information pertaining to both encoded and decoded bits.
- We propose a beneficial realisation of the three-stage serial concatenated scheme, in which the outer code is constituted by the recently introduced Unary Error Correction (UEC) joint source and channel code [24], the middle code is the 5G NR polar code, and the inner component is a 2×2 MIMO detector.
- Furthermore, we present the Three-Dimensional (3D) Extrinsic Information Transfer (EXIT) chart analysis of polar codes for the first time, in order to offer an insight into the iterative convergence of three decoders, as they iteratively exchange soft extrinsic information.
- Furthermore, the Symbol Error Rate (SER) vs. complexity of the proposed hybrid polar decoder is characterised and compared to various soft- and hard-decision output benchmarks, as well as to the relevant three-stage serial concatenated JSCC counterparts and two-stage serial concatenated Separate Source Channel Coding (SSCC) schemes.
- We demonstrate that in comparison to a three-stage serial concatenated JSCC benchmark, the proposed SISO scheme offers 11% complexity reduction compared to the state-of-the-art SISO Soft Cancellation (SCAN) polar decoder, while achieving a similar SER performance. Additionally, the proposed SISO scheme achieves a 0.75 dB SNR gain over the SCAN polar decoder in a two-stage serial concatenated SSCC benchmark.

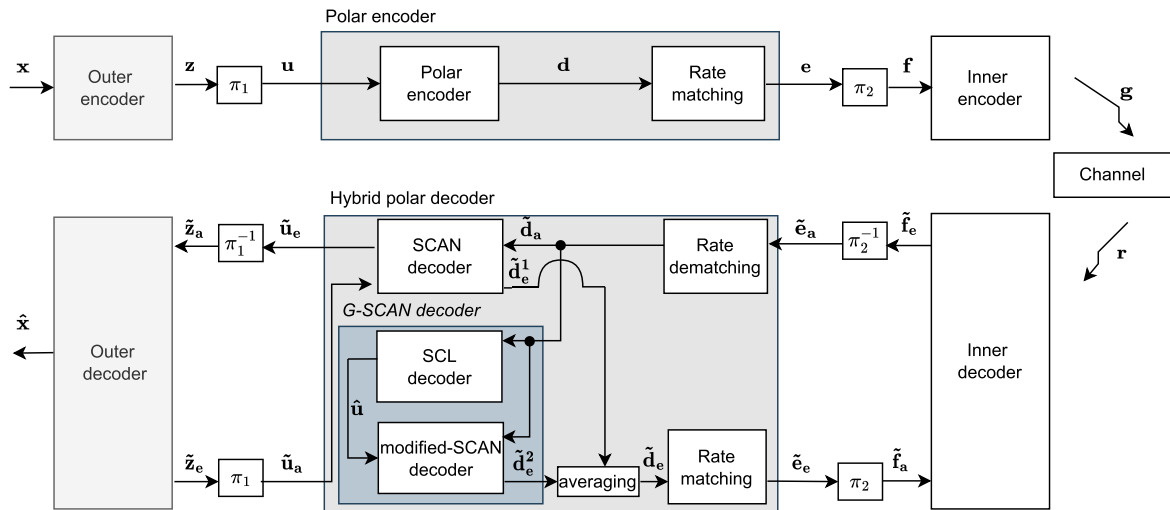


FIGURE 1. Detailed block diagram of the proposed hybrid polar decoder in the context of a three-stage serial concatenated scheme, where the first stage is an outer decoder, the second stage is a hybrid polar decoder, and the third stage is an inner decoder.

The rest of the article is organized as follows. Section II introduces the proposed hybrid polar decoder, while Section III highlights our novel three-stage serial concatenated scheme. Following this, Section IV presents various soft- and hard-decision benchmarks. Sections V and VI discuss our novel EXIT charts and the complexity of the proposed scheme and benchmarks, respectively. Then, Section VII characterises the SER performance of the proposed hybrid decoder and compares it to various JSCC and SSCC schemes. Finally, Section VIII offers our conclusions.

II. PROPOSED HYBRID POLAR DECODER

In this section, a novel hybrid polar decoder is proposed, which has two main components that operate simultaneously, namely an upper SCAN polar decoder [12], and a lower G-SCAN polar decoder [21], as shown in Fig. 1. Here, the G-SCAN polar decoder comprises a conventional SCL decoder [11] which outputs a hard-decision bit vector $\hat{\mathbf{u}}$, as well as a modified-SCAN decoder, which is capable of exploiting $\hat{\mathbf{u}}$ in order to improve the error correction capability [21]. In this way, the G-SCAN decoder achieves superior hard-decision performance over the SCL decoder and outperforms the soft-in soft-out SCAN decoder [21]. In the proposed hybrid decoder the upper SCAN decoder and the lower G-SCAN decoder beneficially complement each other. More specifically, the SISO SCAN decoder is capable of exploiting both the decoded *a-priori* Logarithmic-Likelihood Ratio (LLR)s $\tilde{\mathbf{u}}_a$ and the encoded *a-priori* LLRs $\tilde{\mathbf{d}}_a$ in order to generate the decoded extrinsic LLRs $\tilde{\mathbf{u}}_e$ and the encoded extrinsic LLRs $\tilde{\mathbf{d}}_e$. However, it has limited error correction capability even when performing multiple internal iterations I_{inner}^{max} , which requires relatively high complexity.

By contrast, the G-SCAN decoder offers superior error correction capability at lower complexity than the SISO SCAN decoder, even when performing only a single internal iteration within its modified-SCAN component. However, it is not

suitable for iterating with a concatenated outer decoder, since it cannot accept decoded *a-priori* LLRs $\tilde{\mathbf{u}}_a$. In the proposed hybrid polar decoder we exploit the complementary advantages of the SCAN and the G-SCAN decoders in order to compensate for each other's disadvantages. To elaborate further, this hybrid polar decoder enables the iterative exchange of decoded extrinsic LLRs $\tilde{\mathbf{u}}_e$ between the SCAN polar decoder with an outer decoder, as well as the iterative exchange of encoded extrinsic LLRs $\tilde{\mathbf{d}}_e$ between the high-performance yet low complexity G-SCAN polar decoder with an inner decoder.

In particular, when the hybrid polar decoder is concatenated with an inner and an outer decoder as illustrated in Fig. 1, the iterative decoding process starts with the inner decoder. Here, the inner decoder uses the signal \mathbf{r} received from the channel, as well as the *a-priori* LLR vector $\tilde{\mathbf{f}}_a$, in order to generate the extrinsic LLR vector $\tilde{\mathbf{f}}_e$. Note that, the *a-priori* LLRs in the vector $\tilde{\mathbf{f}}_a$ are initialized to zero for the first iteration. Next, the order of the extrinsic LLRs in the vector $\tilde{\mathbf{f}}_e$ would be rearranged by the deinterleaver π_2^{-1} , in order to generate the E number of *a-priori* LLRs in the vector $\tilde{\mathbf{e}}_a$ as the input of the rate-dematching component. Here, the deinterleaving operation π_2^{-1} employs the reverse interleaving pattern used by the interleaver π_2 in the transmitter. Then, rate-dematching is applied to the E number of *a-priori* LLRs in the vector $\tilde{\mathbf{e}}_a$ in order to generate N *a-priori* LLRs in the vector of $\tilde{\mathbf{d}}_a$, as shown in Fig. 1.

Following that, the decoding process of the hybrid polar decoder of Fig. 1 begins with the operation of the SCAN decoder, which takes its inputs from the encoded *a-priori* LLR vector $\tilde{\mathbf{d}}_a$, as well as from the decoded *a-priori* LLR vector $\tilde{\mathbf{u}}_a$, which is provided by the outer decoder. Note that, during the first iteration, each of the decoded *a-priori* LLRs in $\tilde{\mathbf{u}}_a$ is initialized depending on the frozen bit pattern, which is known by both the transmitter and by the receiver, where an infinite-valued LLR is adopted if it corresponds to a frozen

bit, and a zero-valued LLR is adopted if it corresponds to an information bit. Observe in Fig. 1 that the SCAN decoder processes the inputs of *a-priori* LLR vector $\tilde{\mathbf{d}}_a$ and the *a-priori* LLR vector $\tilde{\mathbf{u}}_a$, in order to generate the decoded extrinsic LLR vector $\tilde{\mathbf{u}}_e$.

Following the operation of the SCAN decoder, the order of the decoded extrinsic LLRs in the vector $\tilde{\mathbf{u}}_e$ is rearranged by the deinterleaver π_1^{-1} , in order to generate the *a-priori* LLR vector $\tilde{\mathbf{z}}_a$, which will then be input to the outer decoder of Fig. 1. As before, the deinterleaving operation π_1^{-1} uses the reverse interleaving pattern of the corresponding interleaver π_1 in the transmitter. Based on the *a-priori* LLR vector $\tilde{\mathbf{z}}_a$, the outer decoder generates the extrinsic LLR vector $\tilde{\mathbf{z}}_e$ of Fig. 1. Following this, the order of the extrinsic LLRs in the vector of $\tilde{\mathbf{z}}_e$ is rearranged by the interleaver π_1 , in order to generate the decoded *a-priori* LLR vector $\tilde{\mathbf{u}}_a$, which will be taken as its input by the upper polar component of the hybrid polar decoder in order to pass on the iteration gain offered by the outer decoder, as seen in Fig. 1. The SCAN decoder also generates a vector of encoded extrinsic LLRs $\tilde{\mathbf{d}}_e^1$ by processing the input *a-priori* LLR vector $\tilde{\mathbf{d}}_a$ and the *a-priori* LLR vector $\tilde{\mathbf{u}}_a$. This SCAN encoded extrinsic LLR output $\tilde{\mathbf{d}}_e^1$ will be combined with the output of the lower G-SCAN decoder through averaging, as it will be detailed in this section.

In parallel with this, the lower component of the hybrid polar decoder is operated, namely, the G-SCAN decoder [21], which takes the same encoded *a-priori* LLR vector $\tilde{\mathbf{d}}_a$ in order to generate a second encoded extrinsic LLR vector $\tilde{\mathbf{d}}_e^2$, using two steps, as shown in Fig. 1. More explicitly, the first step in each operation comprises the operation of the SCL algorithm having a list size of L [11], in order to generate a hard-decision vector of decoded bits $\tilde{\mathbf{u}}$, which selects the best block of decoded bits among a list of L candidates. Then, a second step entails a single internal iteration $I_{inner}^{\max} = 1$ performed by a modified-SCAN algorithm, which accepts the b bits of the decoded vector $\tilde{\mathbf{u}}$ as an input. This is then interleaved with $(N - b)$ frozen bits, as well as the vector of N encoded *a-priori* LLR $\tilde{\mathbf{d}}_a$ in order to generate a vector $\tilde{\mathbf{d}}_e$ of N encoded extrinsic LLRs. Following that, in order to generate a vector $\tilde{\mathbf{d}}_e$ of N encoded extrinsic LLRs, the average of the extrinsic LLRs provided by the SCAN and the G-SCAN decoder may be obtained according to $\tilde{\mathbf{d}}_e = (\tilde{\mathbf{d}}_e^1 + \tilde{\mathbf{d}}_e^2)/2$, as seen in Fig. 1. Following this, the N encoded extrinsic LLRs in the vector $\tilde{\mathbf{d}}_e$ are processed by the rate-matching block of Fig. 1, in order to generate the E encoded extrinsic LLRs of the vector $\tilde{\mathbf{e}}_e$. For further information regarding the schedule and equations of the G-SCAN polar decoder, please refer to [21].

Again, the order of the encoded extrinsic information output LLRs in the vector $\tilde{\mathbf{e}}_e$ is rearranged by the interleaving operation π_2 of Fig. 1, in order to generate the *a-priori* LLR vector $\tilde{\mathbf{f}}_a$, which may be taken as its input by the inner decoder in the next decoding iteration. As shown in Fig. 1, in the successive iterations, the hybrid decoder will process more accurate encoded *a-priori* LLRs of the vector $\tilde{\mathbf{e}}_a$, as well as more accurate decoded *a-priori* LLRs of the vector $\tilde{\mathbf{u}}_a$, which may

be exchanged iteratively with the inner and the outer decoders according to decoding schedule of the inner decoder, SCAN decoder, outer decoder, and the G-SCAN decoder. Note that, the notation of UEC-hybrid(2, L=4)-MIMO indicates the upper SCAN polar decoder component of the proposed hybrid polar decoder employs $I_{inner}^{\max} = 2$ internal iterations, while the lower G-SCAN polar decoder component has a list size of $L = 4$. As will be detailed in the next sections, the proposed hybrid polar decoder imposes lower complexity than using a scheme that relies on SCAN decoding for both the upper and lower polar decoders, while providing 0.25 dB SNR gain as detailed in Section VII.

Note that the performance of the hybrid polar decoder may be further enhanced in some applications by appending a Cyclic Redundancy Check (CRC) to the bit vector \mathbf{u} before performing polar encoding. In the receiver, this CRC may be exploited by the SCL decoder in order to perform CRC-aided SCL decoding (CA-SCL), as detailed in [1]. Note that, further modification is required in this case to remove the LLRs that pertain to CRC bits from the extrinsic LLRs vector $\tilde{\mathbf{u}}_e$, as well as to append zero-valued LLRs to represent the CRC bits in the *a-priori* LLR vector $\tilde{\mathbf{u}}_a$. For further information on the comparison between the CRC-aided-SCL and CRC-aided-G-SCAN algorithms in a two-stage serially concatenated scheme please see [21].

III. SYSTEM OVERVIEW

This section introduces a novel three-stage concatenated scheme, which demonstrates how polar coding can iteratively exchange extrinsic soft information with the relevant inner and outer code. More specifically, Fig. 2 shows the outer JSCC decoder, which is a useful application for example in an outer video decoder, in our three-stage concatenated receiver. In particular, we adopt the recently proposed UEC [24] code, which is capable of near-capacity operation at modest complexity for source symbols selected from an infinite cardinality set, such as in the example of video encoding [24]. Meanwhile, the inner decoder is provided by a MIMO detector, which is a potent application for inner decoding in three-stage serial concatenated receivers. More specifically, we adopt a Gray-mapped 2×2 Quadrature Phase Shift Keying (QPSK) MIMO scheme, which we use for communicating over an uncorrelated narrowband Rayleigh fading channel. Here, the spatial multiplexing MIMO scheme subdivides the data streams into two independent sub-streams, which are mapped onto a pair of transmit antennas. Note that, because this is a joint source-channel coding application, such applications have a tolerance to residual bit and symbols errors, so there is no need to use CRC bits. Hence, for the proposed scheme of Fig. 2, we choose not to adopt a CRC-aided polar decoding algorithm. The signal received from the two receiver antennas is then detected under the assumption of having perfect channel knowledge, with no feedback to the transmitter [28]. The details of the transmitter and receiver design of the proposed three-stage concatenated scheme will be provided in Section III-A and Section III-B, respectively.

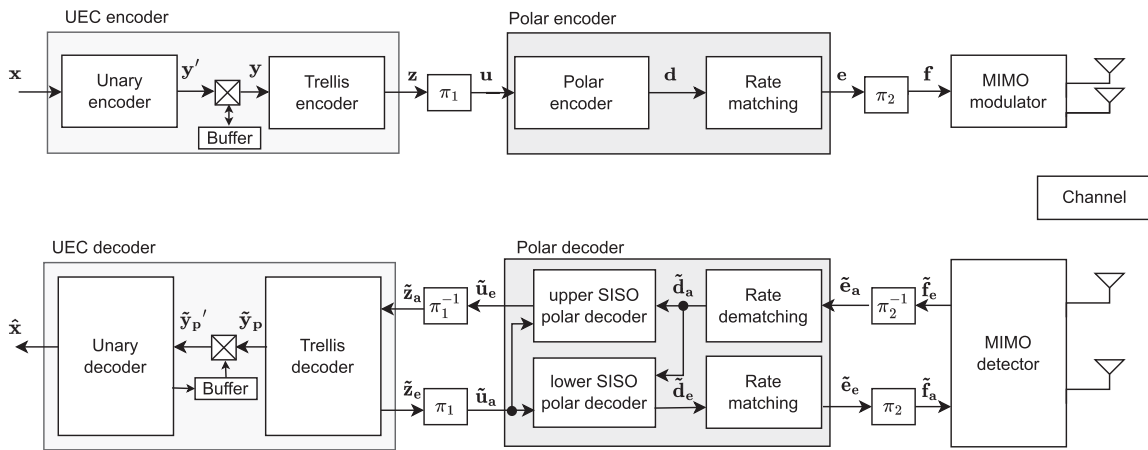


FIGURE 2. Block diagram of a three-stage serial concatenated scheme, where a UEC code is serially concatenated with a SISO polar code and a 2×2 QPSK MIMO modulator and the demodulator.

A. TRANSMITTER

As shown in Fig. 2, the transmitter of the proposed three-stage concatenated scheme is comprised of three encoders, namely the UEC encoder, polar encoder, and MIMO modulator. The UEC encoder consists of two main components, namely the unary encoder and the trellis encoder, as detailed in [24]. The encoding process of Fig. 2 begins with the UEC encoder taking a vector comprising a number of symbols $\mathbf{x} = [x_i]_{i=1}^a$, where each symbol x_i is a realisation of a corresponding random variable X_i , which adopts a symbol value from the infinite cardinality set comprising all positive integers $\mathbb{N}_1 = \{1, 2, 3, \dots\}$, according to the probability distribution of $\Pr(X_i = x) = P(x)$ [24]. Here, we consider the specific example, where the source obeys the zeta distribution, which is defined as

$$P(x) = \frac{x^{-s}}{\zeta(s)}, \tag{1}$$

where $s > 1$ is a parameter of the distribution and $\zeta(s)$ is the Riemann zeta function obeying

$$\zeta(s) = \sum_{x \in \mathbb{N}_1} x^{-s}. \tag{2}$$

Alternatively, the distribution can be parameterized by $p_1 = 1/\zeta(s)$, which quantifies the probability of a zeta-distributed symbol adopting the value of 1, according to $p_1 = \Pr(X_i = 1)$. In the case of zeta distribution, the symbol entropy is given by

$$H_x = \frac{\ln[\zeta(s)]}{\ln(2)} - \frac{s\zeta'(s)}{\ln(2)\zeta(s)}, \tag{3}$$

where $\zeta'(s) = \sum_{x \in \mathbb{N}_1} \ln(x)x^{-s}$ represents the derivative of the Riemann zeta function [24].

Table 2 exemplifies the first ten codewords of the unary encoder, which corresponds to the first ten symbols of \mathbb{N}_1 [24], together with the corresponding probabilities of occurrence for the case of zeta distributions having three example parameterizations of $p_1 = \{0.7, 0.8, 0.9\}$. For example, the symbol $x_i = 5$ corresponds to the unary encoded codeword $y'_i =$

TABLE 2. First Ten Codewords of the Unary Encoder, as Well as the Corresponding Symbol Probabilities for the Case of Zeta Distribution Having the Parameter $p_1 = \{0.7, 0.8, 0.9\}$

Symbol x_i	Probability $P(x_i)$			Unary Codeword y'_i
	$p_1 = 0.7$	$p_1 = 0.8$	$p_1 = 0.9$	
1	0.7000	0.8000	0.9000	1
2	0.1414	0.1158	0.0717	01
3	0.0555	0.0374	0.0163	001
4	0.0286	0.0168	0.0057	0001
5	0.0171	0.0090	0.0025	00001
6	0.0112	0.0054	0.0013	000001
7	0.0079	0.0035	0.0007	0000001
8	0.0058	0.0024	0.0004	00000001
9	0.0044	0.0017	0.0003	000000001
10	0.0034	0.0013	0.0002	0000000001
\vdots	\vdots	\vdots	\vdots	\vdots

[00001]. In this manner, the symbols of \mathbf{x} are mapped to unary codewords, which are concatenated in order to obtain unary encoded bit vector $\mathbf{y}' = [y'_j]_{j=1}^b$ [24], which has a length of b . For example, when the source symbol vector comprises $a = 5$ symbols, such as $\mathbf{x} = [2, 1, 3, 1, 1]$, we obtain the $b = 8$ -bit unary encoded vector $\mathbf{y}' = [01100111]$. In the case of zeta distribution, the average unary codeword length l [24] can be expressed as

$$l = \frac{\zeta(s-1)}{\zeta(s)}. \tag{4}$$

In the case of the example parametrisation of $p_1 = \{0.7, 0.8, 0.9\}$, the average unary codeword length is given by $l = \{2.69, 1.51, 1.16\}$, respectively. Note that, upon using the unary code for zeta distributed symbols, l only remains finite for the case of $s > 2$ and hence $p_1 > 0.698$ [24].

Note that, the length b of the bit sequence of \mathbf{y}' varies from block to block and it has been shown that the SER performance of the UEC is dominated by the shortest block

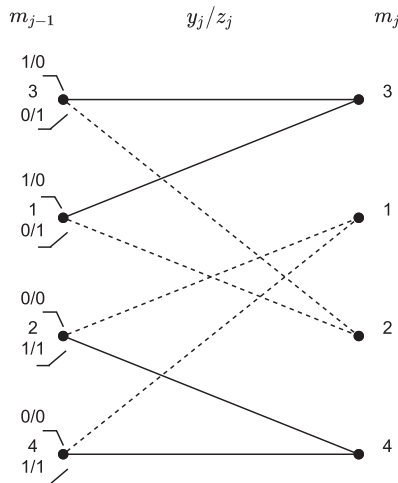


FIGURE 3. $r = 4$ state $n = 1$ -bit UEC trellis.

length [29]. This may be explained by the typical behavior of iterative receiver schemes in which superior performance is obtained when using longer blocks. In order to mitigate this, we adopt the fixed block length method proposed in [29]. This technique has the benefit of improved SER performance, as well as having the fixed block length which enables the interleaver π_1 shown in Fig. 2 to adopt a constant design that does not change from block to block, hence avoiding the potentially excessive memory requirements of storing diverse interleaver designs [29].

To elaborate further, a buffer is placed after the unary encoder, which stores the remaining part of any codeword b that extends past the fixed interleaver length p . For example, in the case of a fixed interleaver length of $p = 4$, the concatenated unary encoded codeword $\mathbf{y}' = [01100111]$ may be decomposed into two consecutive frames, according to $\mathbf{y1} = [0110]$ and $\mathbf{y2} = [0111]$. Note that, in this example, the codeword that corresponds to the third symbol of \mathbf{x} is split between $\mathbf{y1}$ and $\mathbf{y2}$. In this case, the part of this codeword appearing in $\mathbf{y1}$ is stored in the buffer between the generation of $\mathbf{y1}$ and $\mathbf{y2}$. More explicitly, until finishing the transmission of the first frame $\mathbf{y1} = [0110]$, $\mathbf{y2} = [0111]$ must wait in the buffer.

Following unary encoding, each successive frame \mathbf{y} is forwarded to the trellis encoder of Fig. 2. The UEC trellis is parametrized by its number of states r and the number of output bits n generated by each trellis stage, where $r \geq 2$ and $n \geq 1$. A trellis encoder is exemplified in Fig. 3 for the case of $r = 4$ states and $n = 1$ output bits. As it will be detailed in Section VI, $r = 4$ states are chosen to strike a performance vs. complexity trade-off for the UEC decoder. Furthermore, $n = 1$ is chosen, since the additional error correction that would be afforded by using $n \geq 2$ would be made redundant by the concatenated polar code, which has strong error correction performance.

Before encoding each frame \mathbf{y} , the trellis encoder is initialised to the start state of $m_0 = 1$ [24]. Each successive bit y_j of the frame \mathbf{y} is considered by the trellis encoder in

order of increasing index j , and stimulates a transition in the trellis from its previous state $m_{j-1} \in \{1, 2, \dots, r\}$ to a next state $m_j \in \{1, 2, \dots, r\}$ according to

$$m_j = \begin{cases} 1 + \text{odd}(m_{j-1}), & \text{if } y_j = 1 \\ \min[m_{j-1} + 2, r - \text{odd}(m_{j-1})], & \text{if } y_j = 0. \end{cases} \quad (5)$$

Including the start state of $m_0 = 1$, the path identified through the UEC trellis traverses through $p + 1$ states as exemplified in Fig. 3, which shows how synchronization is maintained between the unary encoded symbols and the trellis path [24]. By extending the previous buffer example, the paths traversed through in the trellis for each consecutive frame $\mathbf{y1}$ and $\mathbf{y2}$ can be represented by the vectors $\mathbf{m1} = [1, 3, 2, 1, 3]$ and $\mathbf{m2} = [1, 3, 2, 1, 2]$, respectively. Following this, the trellis encoder converts each unary encoded bit y_j into an n -bit UEC encoded codeword z_j depending on the specific path selected through the UEC trellis. The UEC encoded bits are then concatenated, in order to obtain a $b \cdot n$ -bit UEC encoded vector $\mathbf{z} = [z_k]_{k=1}^{b \cdot n}$. In the example above, we obtain the two consecutive frames $\mathbf{z1} = [0100]$ and $\mathbf{z2} = [0101]$. Note that, the UEC encoded bit vector \mathbf{z} is guaranteed to contain equiprobable binary values if the codewords mapped onto the top and bottom halves of the UEC trellis adopt complementary values [24]. For example, the transition from state $m_{j-1} = 3$ to state $m_j = 3$ in Fig. 3 is associated with an encoded bit value of $z_j = 0$, which is the complement of the transition mirrored in the bottom half of the trellis from state $m_{j-1} = 4$ to state $m_j = 4$ which is associated with an encoded bit value of $z_j = 1$. Hence, the average coding rate of the outer UEC encoder R_o is given by [24]

$$R_o = \frac{H_x}{l \cdot n}. \quad (6)$$

Following the UEC trellis encoding, the order of the bits in the UEC-encoded frame \mathbf{z} is rearranged by the fixed-length interleaving operation π_1 of Fig. 2, in order to obtain the interleaved UEC encoded frame \mathbf{u} . Note that once the interleaving operation of π_1 is complete, the bit vector \mathbf{u} no longer represents a sequence of UEC codewords. From the perspective of the polar encoder, \mathbf{u} simply represents a sequence of bits. As an example, the frames $\mathbf{z1}$ and $\mathbf{z2}$ may be interleaved by the interleaver pattern $\pi_1 = [3, 2, 4, 1]$ in order to obtain the interleaved UEC-encoded frames $\mathbf{u1} = [0100]$ and $\mathbf{u2} = [0110]$. After this interleaving operation, polar encoding is applied to the UEC encoded frame \mathbf{u} , in order to obtain the polar encoded frame \mathbf{d} of Fig. 2. In the example of the input vectors of $\mathbf{u1} = [0100]$ and $\mathbf{u2} = [0110]$ we may obtain $N = 8$ polar encoded output bits $\mathbf{d1} = [11001100]$ and $\mathbf{d2} = [0110110]$, respectively, when using the frozen bit pattern $[0, 0, 0, u_1, 0, u_2, u_3, u_4]$. Here, N represents the encoded block length, which must be a power of 2. Following this, flexible coding block lengths are supported by applying, rate matching to adjust the length of the polar encoded frame from N to E bits, giving a polar coding rate of $R_i = b \cdot n/E$. Then, the order of the E bits in the rate-matched frame \mathbf{e} are rearranged by using the second interleaving operation π_2 of Fig. 2

TABLE 3. Parameters of the Proposed Three-Stage Concatenated UEC-Polar-2 × 2 QPSK MIMO Scheme When Communicated Over an Uncorrelated Rayleigh Fading Channel

p_1	r	s	l	H_X	n	R_o	R_i	$\eta = 2 \cdot R_o$	E_b/N_0 [dB] capacity bound
0.797	2	2.7705	1.5368	1.1708	1	0.7618	0.5	1.5236	-2.26
	4								
	6								
	8								

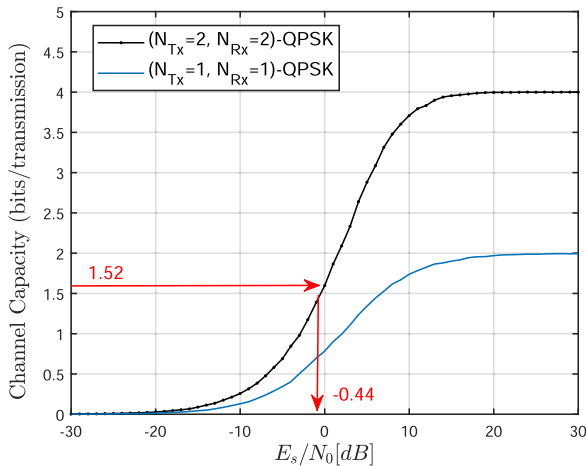


FIGURE 4. Discrete-input Continuous-output Memoryless Channel (DCMC) capacity of an uncorrelated Rayleigh fading channel for a 2 × 2 QPSK MIMO scheme, where N_{Tx} and N_{Rx} represent the number of the transmit and receiver antennas, respectively.

in order to obtain the interleaved frame \mathbf{f} . Following this, a Gray-mapped 2 × 2 QPSK MIMO scheme may be employed for communication over an uncorrelated narrowband Rayleigh fading channel, as shown in Fig. 2.

The effective throughput η of this three-stage serially concatenated scheme may be quantified in terms of bits per transmission, according to

$$\eta = R_o \cdot R_i \cdot \log_2(M) \cdot N_{Tx} \quad (7)$$

where N_{Tx} is the number of transmit antennas, R_o is the coding rate of the UEC scheme, R_i is the coding rate of the rate-matched polar code, and M is the modulation order, which is $M = 4$ for QPSK modulation. More specifically, the throughput of the transmitter in Fig. 2 is given by $\eta = 2 \cdot R_o$ bits/transmission, when $R_i = 1/2$ and 2 × 2 QPSK MIMO modulation are applied.

Fig. 4 plots the Discrete-input Continuous-output Memoryless Channel (DCMC) capacity for 2 × 2 QPSK modulated MIMO transmission over the uncorrelated narrowband Rayleigh fading channel, which provides a theoretical upper bound for reliable communication in the proposed scheme [29], [30]. Here, E_b/N_0 is expressed as

$$E_b/N_0[\text{dB}] = E_s/N_0[\text{dB}] - 10 \cdot \log_{10}(\eta). \quad (8)$$

As an example, the effective throughput becomes $\eta = 2 \cdot R_o = 1.52$ bits/transmission when $p_1 = 0.797$, and $R_o =$

0.7618, as shown in Table 3. As seen in Fig. 4, the effective throughput of $\eta = 1.52$ bits/transmission is achieved at $E_s/N_0 = -0.44$ [dB]. Hence, the capacity bound may be calculated as $E_b/N_0[\text{dB}] = -0.44$ [dB] $- 10 \cdot \log_{10}(1.5236) = -2.26$ [dB], as shown in Table 3.

B. RECEIVER

Upon receiving a frame, the receiver of the three-stage concatenated scheme of Fig. 2 carries out an iterative decoding, in which the MIMO detector, polar decoder and UEC decoder iteratively exchange their extrinsic LLRs. More specifically, each iteration adopts a decoder activation order of {MIMO, upper polar component, UEC, lower polar component}. Hence, the MIMO detection and the UEC decoding are performed once per iteration, and polar decoding is performed twice per iteration.

To elaborate further, the iterative decoding process of Fig. 2 begins with the operation of 2 × 2 QPSK MIMO detection. Here, the 2 × 2 QPSK MIMO detector processes the received signal \mathbf{r} provided by the channel, as well as the *a-priori* LLR vector $\tilde{\mathbf{f}}_a$. Note that, the *a-priori* LLR vector $\tilde{\mathbf{f}}_a$ is populated by zero-valued LLRs at the beginning of the first decoding iteration. During each iteration, the 2 × 2 QPSK MIMO detector generates the extrinsic LLR vector $\tilde{\mathbf{f}}_e$.

The order of the extrinsic LLRs in the vector $\tilde{\mathbf{f}}_e$ are rearranged by the deinterleaver π_2^{-1} , which adopts the reverse of the interleaving pattern π_2 used in the transmitter. The result in the vector of E *a-priori* LLRs $\tilde{\mathbf{e}}_a$ is then provided as the input of the polar decoder’s rate-dematching component shown in Fig. 2. Then, rate-dematching converts the vector of E *a-priori* LLRs $\tilde{\mathbf{e}}_a$ into a vector of N *a-priori* LLRs $\tilde{\mathbf{d}}_a$. Following this, the scheme of Fig. 2 activates the SISO polar decoder, which comprises two separate polar decoding components, referred to as the upper and the lower polar component, as mentioned above.

According to the prescribed decoding activation order of {MIMO, upper polar component, UEC, lower polar component}, the encoded *a-priori* LLR vector $\tilde{\mathbf{d}}_a$ is entered into the upper polar decoder, which also processes the decoded *a-priori* LLR vector $\tilde{\mathbf{u}}_a$ of Fig. 2. Note that, the decoded *a-priori* LLR vector $\tilde{\mathbf{u}}_a$ comprises N LLRs, which are initialized in the first iteration depending on the frozen bit pattern known by both the transmitter and the receiver. Specifically, an infinite value is adopted if the LLR corresponds to a frozen bit, while a zero-value is adopted if the LLR corresponds to an information bit. In response to the *a-priori* LLR input vectors

$\tilde{\mathbf{d}}_a$ and $\tilde{\mathbf{u}}_a$ of Fig. 2, the upper polar decoder generates the encoded extrinsic LLR vector $\tilde{\mathbf{d}}_e^1$ and the decoded extrinsic LLR vector $\tilde{\mathbf{u}}_e$.

Next, the order of the polar decoded extrinsic LLR vector $\tilde{\mathbf{u}}_e$ is rearranged by the deinterleaver π_1^{-1} in order to generate the *a-priori* LLR vector $\tilde{\mathbf{z}}_a$ of Fig. 2. Similar to the deinterleaver π_2^{-1} , the deinterleaver π_1^{-1} uses the reverse interleaving pattern of the corresponding interleaver π_1 seen at the transmitter of Fig. 2. The *a-priori* LLR vector $\tilde{\mathbf{z}}_a$ is then input to the UEC trellis decoder, which generates the extrinsic LLR vector $\tilde{\mathbf{z}}_e$ in response. Next, the order of the extrinsic LLRs in the vector $\tilde{\mathbf{z}}_e$ is rearranged by the interleaver π_1 in order to generate the polar decoded *a-priori* LLR vector $\tilde{\mathbf{u}}_a$, which is forwarded to both the upper and lower polar decoder components, as mentioned above.

The UEC decoding is followed by the operation of the lower polar decoder. This takes the polar decoded *a-priori* LLR vector $\tilde{\mathbf{u}}_a$, as well as the encoded *a-priori* LLR vector $\tilde{\mathbf{d}}_a$ as its input, and generates the encoded extrinsic LLR vector $\tilde{\mathbf{d}}_e$, as seen in Fig. 2. Next, the N encoded extrinsic LLRs of the vector $\tilde{\mathbf{d}}_e$ is rate-matched in order to generate the E extrinsic LLRs of the vector $\tilde{\mathbf{e}}_e$. The order of the extrinsic LLRs in the vector $\tilde{\mathbf{e}}_e$ is rearranged by the interleaver π_2 , which results in the *a-priori* LLR vector $\tilde{\mathbf{f}}_a$ forwarded to the 2×2 QPSK MIMO detector of Fig. 2. This completes an iteration of the proposed receiver according to the activation schedule of {MIMO, upper polar component, UEC, lower polar component}. Note that, the notation of I_{inner}^{max} relates to the number of internal iterations of the polar decoder, while I^{max} relates to the number of receiver-level iterations carried out between the {MIMO, upper polar component, UEC, lower polar component}.

The iterative decoding process continues for a prescribed number of iterations I^{max} , whereupon the UEC trellis decoder outputs the *a-posteriori* LLR vector $\tilde{\mathbf{y}}_p$. Similar to the transmitter, a buffer is placed between the trellis decoder and the unary decoder of Fig. 2. This buffer enables the *a-posteriori* LLR vector $\tilde{\mathbf{y}}_p$ to be appended to any LLRs remaining from the previous frame. The bits are processed by the UEC decoder sequentially and the one-valued bit encountered by the UEC decoder provides the end of the unary code word, since every unary codeword comprises a series of zero-valued bits followed by a single one-valued bit [29]. In this way, the unary decoder consumes all sequences of positive-valued LLRs followed by a single negative-valued LLR and then interprets the result as a legitimate unary codeword. Allowed by writing any remaining LLRs into the buffer ready to be prepended to the next *a-posteriori* LLR vector of $\tilde{\mathbf{y}}_p$ [29].

Returning to the example given in Section III-A, the first *a-posteriori* LLR vector $\tilde{\mathbf{y}}_p^1 = [\tilde{L}1, \tilde{L}2, \tilde{L}3, \tilde{L}4]$ comprises four LLRs. If the unary decoder is successful in decoding $\tilde{\mathbf{y}}_p^1$, it outputs the symbol vector $\hat{\mathbf{x}}^1 = [2, 1]$, and then places the last LLR value of $\tilde{L}4$ into the buffer [29]. Following this, the UEC trellis provides another *a-posteriori* LLR vector $\tilde{\mathbf{y}}_p^2 = [\tilde{L}5, \tilde{L}6, \tilde{L}7, \tilde{L}8]$. These are then concatenated to the LLR $\tilde{L}4$

stored in the buffer, in order to provide the unary decoder with the *a-posteriori* LLR vector $\tilde{\mathbf{y}}_p^2 = [\tilde{L}4, \tilde{L}5, \tilde{L}6, \tilde{L}7, \tilde{L}8]$. Then, the unary decoder will output the symbol vector $\hat{\mathbf{x}}^2 = [3, 1, 1]$, if it is successful in decoding $\tilde{\mathbf{y}}_p^2$, without any remaining LLRs to be placed into the buffer [29]. Then the symbols vector of $\hat{\mathbf{x}}^1$ and $\hat{\mathbf{x}}^2$ may be concatenated in order to reconstruct the symbol vector $\hat{\mathbf{x}} = [2, 1, 3, 1, 1]$ [29].

IV. SCENARIOS AND BENCHMARKERS

In order to characterise the advantages of the proposed hybrid polar decoder, this section introduces a three-stage serial concatenated JSCC benchmark, as well as a two-stage serial concatenated SSCC benchmark. Furthermore, variations of the schemes are considered to employ diverse polar decoders having both hard- and soft-decision outputs.

A. UEC-SCAN-MIMO BENCHMARKER

This benchmarker adopts the same schematics as the proposed UEC-hybrid-MIMO scheme at Fig. 2. However, rather than adopting the proposed hybrid polar decoder, the upper and the lower polar decoder components are provided by the SCAN decoder in this benchmarker. Note that, the SCAN decoder is adopted because it has been shown to offer reasonable decoding performance at a much lower complexity than the SISO Belief Propagation (BP) polar decoder [12], [26]. As described in Section III, the same fixed decoding activation order of {MIMO, upper polar component, UEC, lower polar component} is employed until reaching the maximum number of receiver-level iterations I^{max} . As in the proposed UEC-hybrid-MIMO scheme, the UEC code uses an $n = 1$ -bit UEC trellis having a fixed number of $r = 4$ -states, as recommended in [22], [31].

In order to consider different scenarios, various numbers of internal iterations I_{inner}^{max} are employed within the SCAN decoder for both the upper and lower polar decoder components. Here, the notation UEC-SCAN(1,2)-MIMO when $I^{max} = 4$ indicates that $I_{inner}^{max} = 1$ iteration is used for the upper SCAN polar decoder, while $I_{inner}^{max} = 2$ iterations are used for the lower SCAN polar decoder when a constant number of receiver-level iterations $I^{max} = 4$ are applied between the three-stage of the UEC decoding, SCAN decoding, and the MIMO detector.

B. UNARY-SCAN-MIMO BENCHMARKER

This is a two-stage serial concatenated SSCC benchmarker, which comprises a unary source code and a polar code that is serially concatenated with a 2×2 QPSK MIMO detector, as shown in Fig. 5. In the transmitter, the unary encoder takes the source symbol vector \mathbf{x} and generates the unary encoded vector of \mathbf{y} , as discussed in Section III. Here, the buffer mechanism described in Section III is employed in order to produce the encoded bit vector \mathbf{y} that has a constant length. In this context, the unary code operates in isolation, without the use of a UEC trellis. As a result of this, the interleaver π_1 reorders the bits in the vector \mathbf{y} , in order to produce the bit vector \mathbf{u} ,

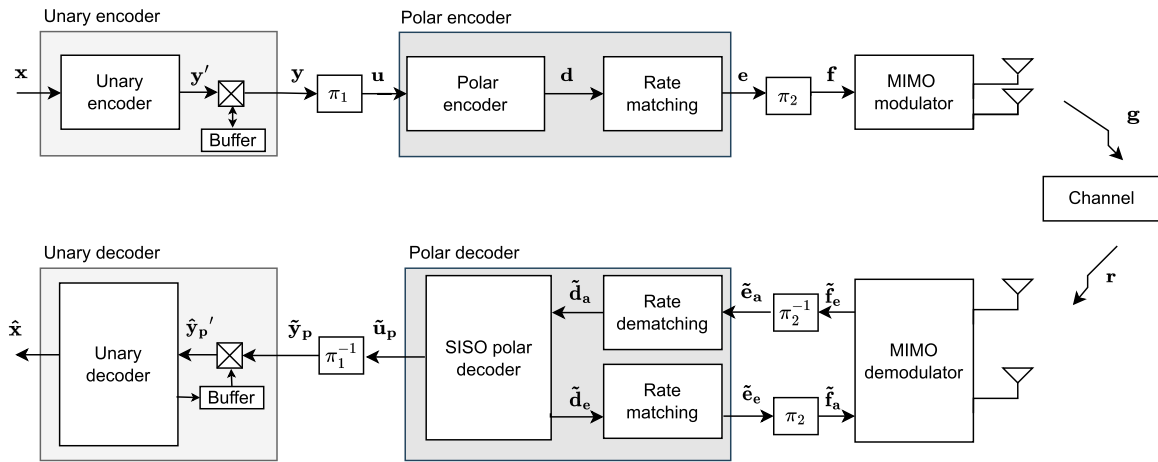


FIGURE 5. Block diagram of a serially concatenated SSCC scheme, where a unary decoder serially concatenated with a SISO polar decoder and a 2×2 QPSK MIMO detector.

which therefore has non-equiprobable values. Hence, when these non-equiprobable bits are channel coded by the polar encoder, some capacity loss may be expected [22]. Following polar encoding, the order of the bits in the polar encoded bit vector \mathbf{e} is rearranged by the interleaver π_2 in order to generate the bit vector \mathbf{f} , which is provided by the 2×2 QPSK MIMO modulation scheme in order to generate the QPSK modulated vector \mathbf{g} . This is then transmitted over an uncorrelated Rayleigh fading channel.

As shown in Fig. 5, the receiver of the Unary-SCAN-MIMO scheme employs a 2×2 QPSK MIMO detector to receive the signal \mathbf{r} from the channel. This is combined with the *a-priori* LLR vector $\tilde{\mathbf{f}}_a$, in order to generate the extrinsic LLR vector $\tilde{\mathbf{f}}_e$, as described in Section III. Following this, the SISO SCAN polar decoder and the 2×2 QPSK MIMO detector iteratively exchange their extrinsic LLR vectors $\tilde{\mathbf{f}}_e$, and $\tilde{\mathbf{e}}_e$ through the deinterleaver π_2^{-1} and interleaver π_2 respectively in order to obtain the *a-priori* LLR vectors $\tilde{\mathbf{e}}_a$ and $\tilde{\mathbf{f}}_a$ as seen in Fig. 5. Here, each operation of the SISO SCAN polar decoder involves I_{inner}^{\max} internal iterations. The iterations between the SISO SCAN polar decoder and the 2×2 QPSK MIMO detector continue until the maximum affordable number of receiver-level iterations I^{\max} is reached, whereupon the SISO SCAN polar decoder generates the *a-posteriori* LLR vector $\tilde{\mathbf{u}}_p$ of Fig. 5. Following this, the order of the *a-posteriori* LLRs in the vector $\tilde{\mathbf{u}}_p$ is rearranged by the deinterleaver π_1^{-1} in order to obtain the *a-posteriori* LLR vector $\tilde{\mathbf{y}}_p$, which is forwarded to the soft-decision unary decoder. This uses the buffer mechanism described in Section III for reconstructing the source symbol vector $\hat{\mathbf{x}}$. Note that, in subsequent discussions, the notation Unary-SCAN(2)-MIMO is adopted, for example, in the case where a maximum of $I_{inner}^{\max} = 2$ internal iterations are used within the SCAN decoder.

C. UNARY-G-SCAN-MIMO BENCHMARKER

The Unary-G-SCAN-MIMO SSCC benchmarker operates in a similar manner to the Unary-SCAN-MIMO benchmarker, with the only difference being that instead of adopting the

SCAN polar decoder is utilized the G-SCAN polar decoder. Here, the G-SCAN decoder is parametrised by the list size L , and the notation Unary-G-SCAN($L=4$)-MIMO indicates that a list size of $L = 4$ is employed for the G-SCAN polar decoder.

D. UNARY-SCL-MIMO BENCHMARKER

This is a non-iterative SSCC benchmarker in which the unary encoder is employed as shown in Fig. 6. Here, the transmitter operates identically to that of the Unary-SCAN-MIMO and the Unary-G-SCAN-MIMO benchmarkers of Fig. 5. However, the receiver differs in terms of the number of iterations employed. Explicitly, once the 2×2 QPSK MIMO detector has received the signal vector \mathbf{r} and has produced the extrinsic LLR vector $\tilde{\mathbf{f}}_e$, ‘one-shot’ polar decoding is employed. More specifically, the order of the LLRs in the vector $\tilde{\mathbf{f}}_e$ is rearranged by the deinterleaver π_2^{-1} in order to obtain the *a-priori* LLR vector $\tilde{\mathbf{e}}_a$. Following this, an SCL polar decoder is employed in order to obtain the decoded bit vector $\hat{\mathbf{u}}_p$. Then, the bits in the vector $\hat{\mathbf{u}}_p$ are rearranged by the deinterleaver π_1^{-1} in order to obtain the bit vector $\hat{\mathbf{y}}_p$. Finally, the unary decoder operates as described in the context of the Unary-SCAN-MIMO and the Unary-G-SCAN-MIMO benchmarkers of Fig. 5, in order to reconstruct the source symbol vector $\hat{\mathbf{x}}$. As an example, the notation of Unary-SCL($L=32$)-MIMO indicates a list size of $L = 32$ is used for the SCL polar decoder.

V. THREE-DIMENSIONAL (3D) EXTRINSIC INFORMATION TRANSFER (EXIT) CHART ANALYSIS

This section characterises the iterative decoding schedule of the proposed three-stage serial concatenated scheme of Section III. A novel 3D EXIT chart analysis [4], [32], [33] is presented, which is capable of visually characterizing the iterative decoding convergence of the proposed system, as well as verifying the correct operation of the proposed algorithms [4], [32], [33]. More explicitly, these 3D EXIT charts characterise the iterative exchange of extrinsic information between the UEC, polar, and the MIMO components of Fig. 2, which adopt

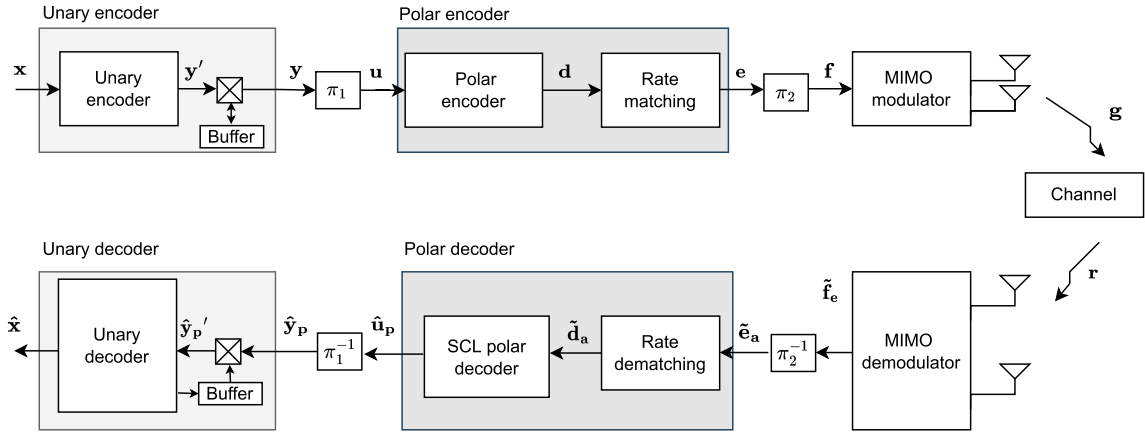


FIGURE 6. Block diagram of a non-iterative SSCC scheme, where a unary decoder is serially concatenated with a SCL polar decoder and a 2×2 QPSK MIMO detector.

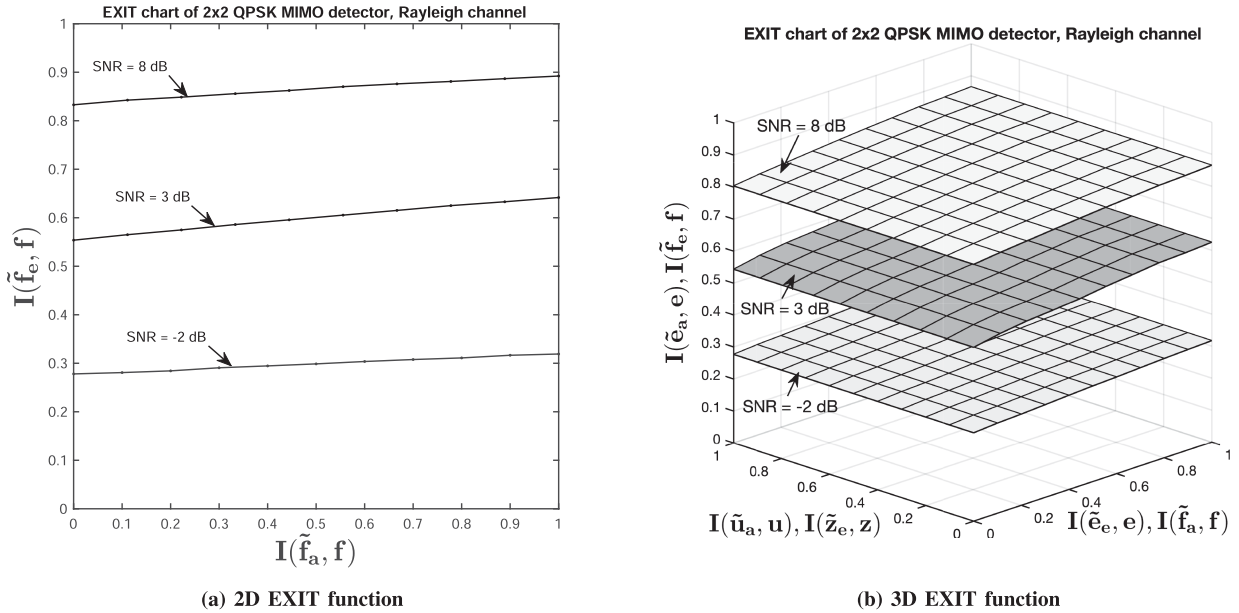


FIGURE 7. (a) 2D and (b) 3D EXIT function characteristics of 2×2 QPSK MIMO detector, when communicated over an uncorrelated narrowband Rayleigh fading channel having SNRs of $\{-2, 3, 8\}$ dB.

the decoder activation order of {MIMO, upper polar component, UEC, lower polar component}. We begin by discussing the EXIT functions of the 2×2 QPSK MIMO detector and of the UEC codes in Section V-A and Section V-B, respectively. Furthermore, we introduce the more complicated EXIT functions of polar codes in Section V-C, before introducing the iterative decoding trajectories between these EXIT functions in Section V-D.

A. EXIT CHART ANALYSIS OF 2×2 QPSK MIMO DETECTOR

In general, the EXIT function of a component can be characterized by quantifying the Mutual Information (MI) of the extrinsic LLR vector at the output of the component [34], as a function of the *a-priori* LLR vector at the input of the component. The 2×2 QPSK MIMO detector of Fig. 2 generates the extrinsic LLR vector $\tilde{\mathbf{f}}_e$, as a function of the corresponding

a-priori LLR vector $\tilde{\mathbf{f}}_a$ as well as of the signal received over the channel \mathbf{r} . More specifically, the MI $\mathbf{I}(\tilde{\mathbf{f}}_e, \mathbf{f})$ of $\tilde{\mathbf{f}}_e$ is related to both the MI $\mathbf{I}(\tilde{\mathbf{f}}_a, \mathbf{f})$ as well as to the channel's Signal-to-Noise Ratio (SNR). Hence, the 2×2 QPSK MIMO detector may be characterized by the EXIT function $\mathbf{I}(\tilde{\mathbf{f}}_e, \mathbf{f}) = \mathbf{F}_{\text{MIMO}}[\mathbf{I}(\tilde{\mathbf{f}}_a, \mathbf{f}), \text{SNR}]$. Fig. 7(a) visualizes the Two-Dimensional (2D) EXIT function of the 2×2 QPSK MIMO detector for various SNR values. As shown in Fig. 7(a), a higher SNR value corresponds to a larger area under the EXIT function of the 2×2 QPSK MIMO detector, which results in a wider open EXIT chart tunnel for reliable communication [33], as we will show in Section V-D.

Note that, the operation of each of the UEC decoder, polar decoder, and the MIMO detector of Fig. 2 is related to one or both of the LLR vector $\tilde{\mathbf{e}}_a$ and the LLR vector $\tilde{\mathbf{u}}_a$. In the case of the MIMO detector, this relationship is related to $\tilde{\mathbf{e}}_a$ and it

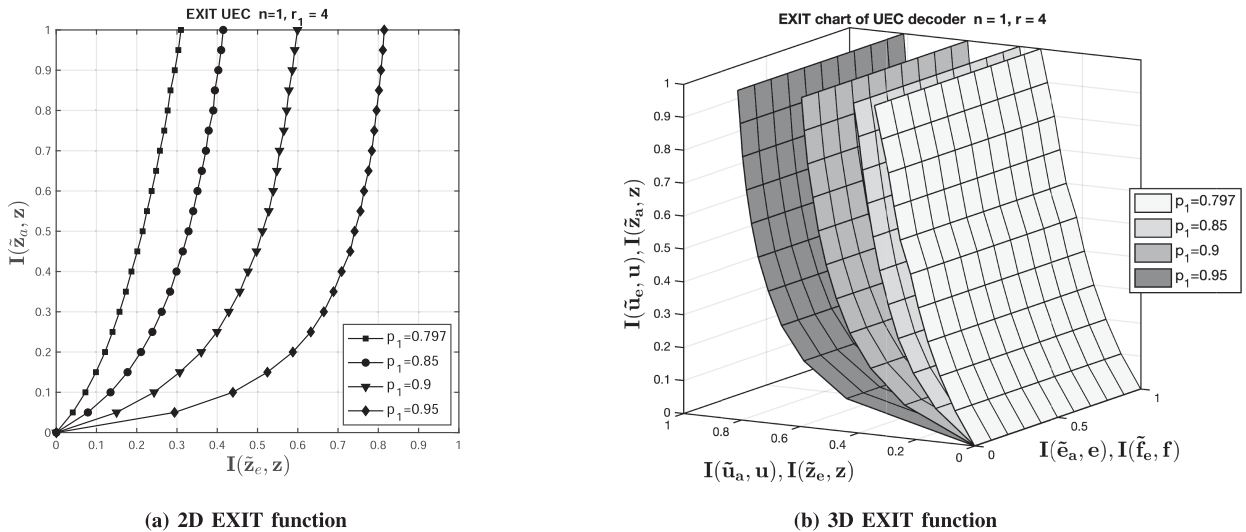


FIGURE 8. (a) 2D and (b) 3D EXIT function of the UEC decoder for different zeta distributed source symbols parameterized by various values of $p_1 = \{0.797, 0.85, 0.9, 0.95\}$, for the case of using $n = 1$ encoded bit per transmission and $r = 4$ -states.

is obtained by deinterleaving the extrinsic LLR vector $\tilde{\mathbf{f}}_e$. In order to jointly characterise the UEC decoder, polar decoder, and the MIMO detector it is beneficial to include $\mathbf{I}(\tilde{\mathbf{u}}_a, \mathbf{u})$ and $\mathbf{I}(\tilde{\mathbf{e}}_a, \mathbf{e})$ in the EXIT function analysis. This motivates the 3D EXIT function plot of Fig. 7(b) in which $\mathbf{I}(\tilde{\mathbf{u}}_a, \mathbf{u})$ is presented on one axis. Furthermore, $\mathbf{I}(\tilde{\mathbf{e}}_a, \mathbf{e})$ is presented on a second axis together with $\mathbf{I}(\tilde{\mathbf{f}}_e, \mathbf{f})$ owing to the relationship established through the deinterleaver π_2^{-1} . Similarly, $\mathbf{I}(\tilde{\mathbf{f}}_e, \mathbf{f})$ appears on a third axis together with $\mathbf{I}(\tilde{\mathbf{e}}_a, \mathbf{e})$ owing to the relationship established through the interleaver π_2 . Note that, the EXIT function of the 2×2 QPSK MIMO detector does not depend on the MI $\mathbf{I}(\tilde{\mathbf{u}}_a, \mathbf{u})$, hence the EXIT function of Fig. 7(b) does not vary along the corresponding axis.

B. EXIT CHART ANALYSIS OF THE UEC DECODER

As shown in Fig. 2, the UEC decoder generates the extrinsic LLR vector $\tilde{\mathbf{z}}_e$ as a function of the *a-priori* LLR vector $\tilde{\mathbf{z}}_a$. Hence, the operation of the UEC decoder may be characterized by the EXIT function $\mathbf{I}(\tilde{\mathbf{z}}_e, \mathbf{z}) = \mathbf{F}_{\text{UEC}}[\mathbf{I}(\tilde{\mathbf{z}}_a, \mathbf{z})]$ [22], [31]. Fig. 8(a) visualizes the 2D EXIT function of the UEC decoder for zeta distributed source symbols parameterized by various values of $p_1 = \{0.797, 0.85, 0.9, 0.95\}$, for the case where the UEC trellis has $n = 1$ encoded bit per transmission and $r = 4$ states. Throughout the remainder of this article, $p_1 = 0.797$ will be adopted, since this maximizes the DCMC capacity, as mentioned in Section III-A. Note that, the 2D EXIT function of the UEC decoder has been extensively explored considering various p_1 and r values in [22], [31]. Note that as detailed in [22], in the case of $n = 1$ the EXIT function of the UEC decoder does not reach $\mathbf{I}(\tilde{\mathbf{z}}_e, \mathbf{z}) = 1$ when $\mathbf{I}(\tilde{\mathbf{z}}_a, \mathbf{z}) = 1$. In the case of a two-stage serial concatenated iterative decoding scheme, this would prevent iterative decoding from having a low decoding error rate. However, since we have a three-stage concatenation with a powerful polar code, we may expect to achieve iterative decoding convergence to a low decoding error rate.

As mentioned above, the operation of each of the UEC decoder, polar decoder, and the MIMO detector of Fig. 2 is related to both the LLR vector $\tilde{\mathbf{e}}_a$ or to the LLR vector $\tilde{\mathbf{u}}_a$. In the case of the UEC decoder, this relationship with $\tilde{\mathbf{u}}_a$ is established by interleaving the extrinsic LLR vector $\tilde{\mathbf{z}}_e$. In order to jointly characterise the UEC decoder, polar decoder, and the MIMO detector it is beneficial to include both $\mathbf{I}(\tilde{\mathbf{u}}_a, \mathbf{u})$ and $\mathbf{I}(\tilde{\mathbf{e}}_a, \mathbf{e})$ in the EXIT function analysis. This motivates the conception of the 3D EXIT function plot of Fig. 8(b) in which $\mathbf{I}(\tilde{\mathbf{e}}_a, \mathbf{e})$ is presented along one axis. Furthermore, $\mathbf{I}(\tilde{\mathbf{u}}_e, \mathbf{u})$ is presented along a second axis together with $\mathbf{I}(\tilde{\mathbf{z}}_a, \mathbf{z})$ owing to the relationship established through the deinterleaver π_1^{-1} . Similarly, $\mathbf{I}(\tilde{\mathbf{u}}_a, \mathbf{u})$ appears on a third axis together with $\mathbf{I}(\tilde{\mathbf{z}}_e, \mathbf{z})$ owing to the relationship created through the interleaver π_1 . Note that, the EXIT function of the UEC decoder does not depend on $\mathbf{I}(\tilde{\mathbf{e}}_a, \mathbf{e})$ and hence the EXIT function of Fig. 8(b) does not vary along the corresponding axis.

C. EXIT CHART ANALYSIS OF THE POLAR DECODER

In general, in the case of SISO polar decoding, there are two extrinsic LLR vector outputs, namely the polar decoded extrinsic LLR vector $\tilde{\mathbf{u}}_e$ and the encoded extrinsic LLR vector $\tilde{\mathbf{e}}_e$. Additionally, the SISO polar decoder has two *a-priori* LLR vector inputs, namely the polar decoded *a-priori* LLR vector $\tilde{\mathbf{u}}_a$ and the encoded *a-priori* LLR vector $\tilde{\mathbf{e}}_a$. The MI of the polar decoded extrinsic LLR vector output $\mathbf{I}(\tilde{\mathbf{u}}_e, \mathbf{u})$ relies not only on the MI of the decoded *a-priori* LLR vector $\mathbf{I}(\tilde{\mathbf{u}}_a, \mathbf{u})$ but also on the MI of the encoded *a-priori* LLR vector $\mathbf{I}(\tilde{\mathbf{e}}_a, \mathbf{e})$. Hence, the MI of decoded extrinsic LLR characteristic of the SISO polar decoder may be expressed as the EXIT function $\mathbf{I}(\tilde{\mathbf{u}}_e, \mathbf{u}) = \mathbf{F}_{\text{decoded-polar}}[\mathbf{I}(\tilde{\mathbf{u}}_a, \mathbf{u}), \mathbf{I}(\tilde{\mathbf{e}}_a, \mathbf{e})]$. Similarly, the MI of the encoded extrinsic LLR vector $\mathbf{I}(\tilde{\mathbf{e}}_e, \mathbf{e})$ of the polar decoder relies not only on the MI of decoded *a-priori* LLR vector $\mathbf{I}(\tilde{\mathbf{u}}_a, \mathbf{u})$, but also on the MI of the encoded *a-priori* LLR vector $\mathbf{I}(\tilde{\mathbf{e}}_a, \mathbf{e})$. Hence, it may be expressed as $\mathbf{I}(\tilde{\mathbf{e}}_e, \mathbf{e}) = \mathbf{F}_{\text{encoded-polar}}[\mathbf{I}(\tilde{\mathbf{e}}_a, \mathbf{e}), \mathbf{I}(\tilde{\mathbf{u}}_a, \mathbf{u})]$. Since each output

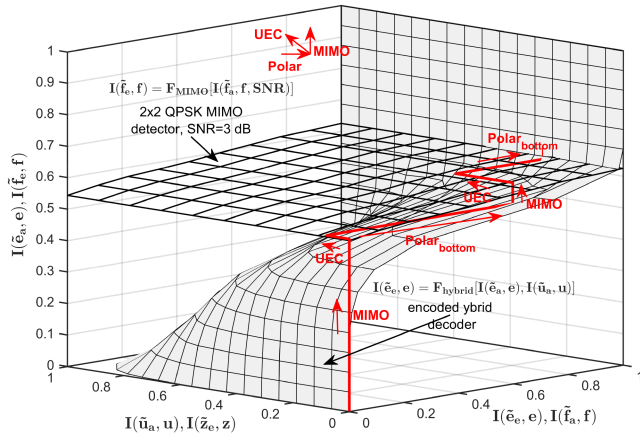


FIGURE 9. 3D EXIT chart characteristics of the proposed encoded hybrid polar decoder from the point of view 2×2 QPSK MIMO detector for the case of transmission over an uncorrelated narrowband Rayleigh fading channel having a SNR = 3 dB, $I_{inner}^{max} = 2$ internal iterations being used within the upper SCAN polar decoder component, and a list size of $L = 4$ being used within the lower G-SCAN polar decoder component.

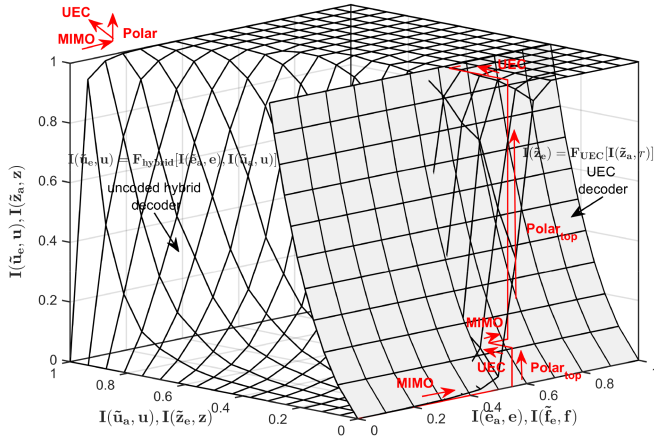


FIGURE 10. 3D EXIT chart characteristics of the proposed hybrid polar decoder from the point of view of the UEC decoder for the case of $r = 4$ states and the zeta distribution parameter of $p_1 = 0.797$.

is a function of two inputs, 3D EXIT functions are required to represent the characteristics of SISO polar decoders.

In the case of the proposed hybrid polar decoder of Fig. 1, the polar decoded extrinsic EXIT function $\mathbf{I}(\tilde{\mathbf{u}}_e, \mathbf{u}) = \mathbf{F}_{\text{unencoded-polar}}[\mathbf{I}(\tilde{\mathbf{u}}_a, \mathbf{u}), \mathbf{I}(\tilde{\mathbf{e}}_a, \mathbf{e})]$ relies on the upper SCAN polar decoder component, while the encoded extrinsic EXIT function $\mathbf{I}(\tilde{\mathbf{e}}_e, \mathbf{e}) = \mathbf{F}_{\text{encoded-polar}}[\mathbf{I}(\tilde{\mathbf{e}}_a, \mathbf{e}), \mathbf{I}(\tilde{\mathbf{u}}_a, \mathbf{u})]$ relies on the lower G-SCAN polar decoder component. Fig. 1. In order to validate the proposed hybrid polar decoder algorithm, the corresponding 3D EXIT chart characteristics are provided in Figs. 9 and 10 for the encoded and decoded extrinsic EXIT functions, respectively.

Note that, the axis plotting $\mathbf{I}(\tilde{\mathbf{e}}_a, \mathbf{e})$ and $\mathbf{I}(\tilde{\mathbf{e}}_e, \mathbf{e})$ are provided together with $\mathbf{I}(\tilde{\mathbf{f}}_e, \mathbf{f})$ and $\mathbf{I}(\tilde{\mathbf{f}}_a, \mathbf{f})$, respectively. This is because the extrinsic LLR vector output by the MIMO detector becomes the encoded *a-priori* LLR vector for the polar decoder and vice versa, where the interleaving and the deinterleaving

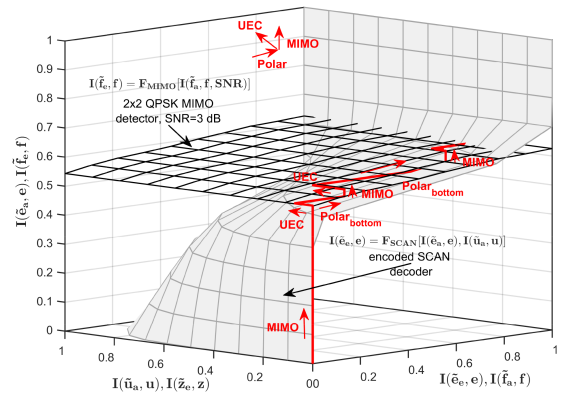


FIGURE 11. 3D EXIT chart characteristics of the UEC-SCAN-MIMO benchmarker from the point of view 2×2 QPSK MIMO detector for the case of transmission over an uncorrelated narrowband Rayleigh fading channel having a SNR = 3 dB, $I_{inner}^{max} = 1$ internal iterations being used within the SCAN polar decoder.

operations do not change the MI. Likewise, the decoded *a-priori* MI $\mathbf{I}(\tilde{\mathbf{u}}_a, \mathbf{u})$ and the decoded extrinsic MI $\mathbf{I}(\tilde{\mathbf{u}}_e, \mathbf{u})$ are provided on the same axis as $\mathbf{I}(\tilde{\mathbf{z}}_e, \mathbf{z})$ and $\mathbf{I}(\tilde{\mathbf{z}}_a, \mathbf{z})$, respectively. This is because the *a-priori* LLR vector of the UEC decoder is provided by the decoded extrinsic LLR vector of the SISO polar decoder and vice versa, where the interleaving and the deinterleaving operations do not change the MI.

Fig. 9 shows the EXIT characteristic of the hybrid polar decoder from the point of view of the 2×2 QPSK MIMO detector, for the case of transmission over an uncorrelated narrowband Rayleigh fading channel having SNR = 3 dB. Here, $I_{inner}^{max} = 2$ internal iterations are used within the upper SCAN polar decoder, and a list size of $L = 4$ is used within the lower G-SCAN polar decoder. Hence, Fig. 9 also includes the EXIT function $\mathbf{I}(\tilde{\mathbf{f}}_e, \mathbf{f}) = \mathbf{F}_{\text{MIMO}}[\mathbf{I}(\tilde{\mathbf{f}}_a, \mathbf{f}), \text{SNR}]$ of the MIMO detector projected in the three dimensions. Furthermore, Fig. 10 shows the EXIT characteristic of the hybrid polar decoder from the point of view of the UEC decoder, for the case of $r = 4$ states and the zeta distribution parameter of $p_1 = 0.797$. Hence, Fig. 10 also includes the EXIT function $\mathbf{I}(\tilde{\mathbf{z}}_e, \mathbf{z}) = \mathbf{F}_{\text{UEC}}[\mathbf{I}(\tilde{\mathbf{z}}_a, \mathbf{z})]$ of the UEC decoder projected in the three dimensions.

For the sake of comparison, Figs. 11 and 12 provide the 3D EXIT characteristics of the UEC-SCAN-MIMO benchmarker of Fig. 2 when $I_{inner}^{max} = 1$ internal iteration is used within the upper and lower SCAN decoders. More specifically, Fig. 11 shows the EXIT characteristic of this benchmarker from the point of view of the 2×2 QPSK MIMO detector for transmission over an uncorrelated narrowband Rayleigh fading channel having SNR = 3 dB. Finally, Fig. 12 shows the EXIT characteristics of the UEC-SCAN-MIMO benchmarker from the point of view of the UEC decoder, when using $r = 4$ states and the zeta distribution parameter of $p_1 = 0.797$.

D. TRAJECTORIES

The proposed three-stage concatenated scheme can be further validated by measuring the MI obtained during an iterative

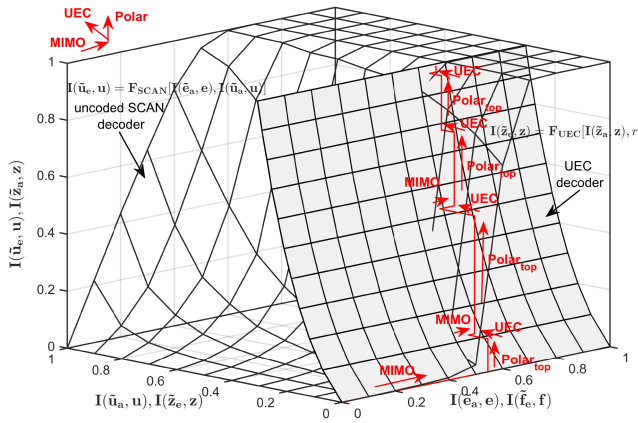


FIGURE 12. 3D EXIT chart characteristics of the UEC-SCAN-MIMO benchmarker from the point of view the UEC decoder for the case of $r = 4$ states and the zeta distribution parameter of $p_1 = 0.797$.

TABLE 4. Example of Measuring the MI Trajectory of the Extrinsic LLRs Obtained During the Particular Simulated Iterative Decoding Process Between the Three-Stage Concatenated UEC-Hybrid polar-MIMO Scheme When Employing a (MIMO, Upper Polar Component, UEC, Lower Polar component) Decoder Activation Order for Two Iterations $I^{\max} = 2$

Iteration	Activation order	$I(\tilde{f}_e, f)$	$I(\tilde{u}_e, u)$	$I(\tilde{z}_e, z)$	$I(\tilde{e}_e, e)$
0	-	0	0	0	0
1	MIMO	0.5484	0	0	0
	upper polar	0.5484	0.1306	0	0
	UEC	0.5484	0.1306	0.0801	0
	lower polar	0.5484	0.1306	0.0801	0.6150
2	MIMO	0.6800	0.1306	0.0801	0.6150
	upper polar	0.6800	1	0.0801	0.6150
	UEC	0.6800	1	0.2825	0.6150
	lower polar	0.6800	1	0.2825	1

decoding process, when employing the {MIMO, upper polar component, UEC, lower polar component} decoder activation order. As an example, Table 4 characterises the iterative exchange of extrinsic information between the components of the proposed three-stage concatenated UEC-hybrid polar decoder-MIMO scheme for up to two iterations. More specifically, when the MIMO detector is activated for the first time using the *a-priori* MI of $I(\tilde{f}_a, f) = 0$, an extrinsic MI of $I(\tilde{f}_e, f) = 0.5484$ is obtained, as highlighted in Table 4. As shown in the block diagram of Fig. 2, the extrinsic LLR vector \tilde{f}_e is passed through the deinterleaver π_2^{-1} in order to obtain the *a-priori* LLR vector \tilde{e}_a , which accordingly has the same MI of $I(\tilde{e}_a, e) = 0.5484$. Hence as shown in both Figs. 9 and 10, the trajectory evolves along the axis label $I(\tilde{e}_a, e), I(\tilde{f}_e, f)$ from the coordinates $[I(\tilde{f}_e, f), I(\tilde{u}_e, u), I(\tilde{z}_e, z), I(\tilde{e}_e, e)] = [0, 0, 0, 0]$ to the coordinates $[I(\tilde{f}_e, f), I(\tilde{u}_e, u), I(\tilde{z}_e, z), I(\tilde{e}_e, e)] = [0.5484, 0, 0, 0]$, as shown in the first two rows of Table 4. Next, this encoded *a-priori* MI of $I(\tilde{e}_a, e) = 0.5484$ is entered into the upper SCAN polar decoder component of the proposed hybrid polar decoder,

together with a decoded *a-priori* MI of $I(\tilde{u}_a, u) = 0$, in order to generate the decoded extrinsic MI of $I(\tilde{u}_e, u) = 0.1306$. As shown in the block diagram of Fig. 2, the decoded extrinsic LLR vector \tilde{u}_e is passed through the deinterleaver π_1^{-1} in order to obtain the decoded *a-priori* LLR vector \tilde{z}_a , which accordingly has the same MI of $I(\tilde{z}_a, z) = 0.1306$. In this way, the trajectory evolves along the axis label $I(\tilde{u}_e, u), I(\tilde{z}_a, z)$, which can only be observed in Fig. 10, since Fig. 9 does not have this axis. Following that, the UEC decoder is activated and the extrinsic MI of $I(\tilde{z}_e, z) = 0.0801$ is obtained, as highlighted in Table 4.

Similarly, as shown in the block diagram of Fig. 2, the extrinsic LLR vector \tilde{z}_e is passed through the interleaver π_1 in order to obtain decoded *a-priori* LLR vector \tilde{u}_a , which accordingly has the same MI of $I(\tilde{u}_a, u) = 0.0801$. Hence, the trajectory evolves along the axis label $I(\tilde{u}_a, u), I(\tilde{z}_e, z)$, as shown in both Fig. 9 and in Fig. 10. Then, the lower G-SCAN polar decoder is activated in order to obtain the encoded extrinsic MI of $I(\tilde{e}_e, e) = 0.6150$. Similarly, as shown in the block diagram of Fig. 2, the encoded extrinsic LLR vector \tilde{e}_e is passed through the interleaver π_2 in order to obtain *a-priori* LLR vector \tilde{f}_a , which accordingly has the same MI of $I(\tilde{f}_a, f) = 0.6150$. In this way, the trajectory evolves along the axis label $I(\tilde{e}_e, e), I(\tilde{f}_a, f)$, which can only be observed in Fig. 9, since Fig. 10 does not have this axis. Once this first iteration is completed, a second iteration begins with a trajectory that evolves again along the axis label $I(\tilde{e}_a, e), I(\tilde{f}_e, f)$, where the MI of $I(\tilde{f}_e, f) = 0.6800$ is obtained, as highlighted in Table 4. This process continues until reaching the maximum affordable number of receiver-level iterations I^{\max} among the three stages.

By plotting the above trajectories between the 3D EXIT surfaces of the hybrid polar decoder and either the 2×2 MIMO detector of Fig. 9 or the UEC decoder of Fig. 10, the iterative decoding process can be validated. As seen in Fig. 9, the corner points of the stair-case-shaped decoding trajectory are in close agreement with both the 3D EXIT surfaces of the encoded hybrid polar decoder and of the 2×2 MIMO detector, which validates the accuracy of our EXIT functions. More specifically, if the trajectory reaches the encoded extrinsic MI of $I(\tilde{e}_e, e) = 1$, then this implies that an open EXIT tunnel exists and that the iterative decoding process converges to low block error rate [33]. The trajectory of Fig. 9 indeed confirms that an open tunnel does exist for the UEC-hybrid polar-MIMO scheme at SNR= 3 dB, reaching the value of $I(\tilde{e}_e, e) = 1$, as shown in Table 4. Similarly, as shown in Fig. 10, the corner points of the stair-case-shaped decoding trajectory are also in close agreement with the 3D EXIT functions of both the decoded hybrid polar decoder and of the UEC decoder. Again, if the trajectory approaches a decoded MI of $I(\tilde{u}_e, u) = 1$, this implies that an open EXIT tunnel exists and that iterative decoding converges to a low block error rate. Similarly to Fig. 9, the trajectory of Fig. 10 confirms that an open tunnel does exist for the UEC-hybrid polar-MIMO scheme, since the decoded extrinsic MI of $I(\tilde{u}_e, u) = 1$ is reached in Table 4.

TABLE 5. Example of Measuring the MI Trajectory of the Extrinsic LLRs Obtained During the Particular Simulated Iterative Decoding Process Between the Three-Stage Concatenated UEC-SCAN-MIMO Scheme When Employing a (MIMO, Upper Polar Component, UEC, Lower Polar component) Decoder Activation Order for Five Iterations $I^{\max} = 5$

Iteration	Activation order	$I(\tilde{\mathbf{f}}_e, \mathbf{f})$	$I(\tilde{\mathbf{u}}_e, \mathbf{u})$	$I(\tilde{\mathbf{z}}_e, \mathbf{z})$	$I(\tilde{\mathbf{e}}_e, \mathbf{e})$
0	-	0	0	0	0
1	MIMO	0.5452	0	0	0
	upper polar	0.5452	0.1166	0	0
	UEC	0.5452	0.1166	0.0718	0
	lower polar	0.5452	0.1166	0.0718	0.2065
2	MIMO	0.5689	0.1166	0.0718	0.2065
	upper polar	0.5689	0.5306	0.0718	0.2065
	UEC	0.5689	0.5306	0.1979	0.2065
	lower polar	0.5689	0.5306	0.1979	0.7607
3	MIMO	0.6228	0.5306	0.1979	0.7607
	upper polar	0.6228	0.7888	0.1979	0.7607
	UEC	0.6228	0.7888	0.2399	0.7607
	lower polar	0.6228	0.7888	0.2399	0.7918
4	MIMO	0.6178	0.7888	0.2399	0.7918
	upper polar	0.6178	0.9809	0.2399	0.7918
	UEC	0.6178	0.9809	0.2826	0.7918
	lower polar	0.6178	0.9809	0.2826	0.9765
5	MIMO	0.6417	0.9809	0.2826	0.9765
	upper polar	0.6417	1	0.2826	0.9765
	UEC	0.6417	1	0.2861	0.9765
	lower polar	0.6417	1	0.2861	1

As shown in Figs. 11 and 12, the corner points of the staircase-shaped decoding trajectory of the UEC-SCAN-MIMO benchmark are also in close agreement with the 3D EXIT surfaces. The corresponding trajectories are exemplified in Table 5. Observe that the proposed hybrid polar decoder has a wide open tunnel between the 3D EXIT surfaces compared to the SCAN polar decoder benchmarked. Hence fewer iterations are required for reaching the $I(\tilde{\mathbf{u}}_e, \mathbf{u}) = 1$ or $I(\tilde{\mathbf{e}}_e, \mathbf{e}) = 1$ points. More specifically, Table 4 shows that only two iterations are required by the UEC-hybrid polar decoder-MIMO scheme to reach the $I(\tilde{\mathbf{u}}_e, \mathbf{u}) = 1$ and $I(\tilde{\mathbf{e}}_e, \mathbf{e}) = 1$ points. By comparison, five iterations are required by the UEC-SCAN-MIMO benchmarked of Fig. 2. Hence, the proposed hybrid polar decoder scheme can be expected to have a better performance than that of the UEC-SCAN-MIMO benchmarked of Fig. 2, as it will be shown in Section VII.

VI. COMPLEXITY ANALYSIS

This section quantifies the computational complexity of the proposed hybrid polar decoder and compares it to that of the relevant JSCC and SSCC benchmarkers. Note that, the 2×2 QPSK MIMO demodulator complexity is identical for all schemes, where the computational complexity of the ML detector is in the order of $\mathcal{O}(M^{N_t})$, which grows exponentially with the number N_{T_x} of transmit antennas and the cardinality

M of the QAM modulated-signal constellation [35]. In this article, $N_{T_x} = 2$ and $M = 4$ are adopted in all the schemes considered. Additionally, in all the JSCC schemes considered, the complexity of the UEC decoder is common and depends on the number of states r used in the UEC trellis, as detailed in [22], [31]. In this article, a UEC trellis having $r = 4$ states is adopted, since this was shown in [22], [31] to be sufficient for avoiding significant capacity loss.

The complexity of a polar decoder can be quantified by considering the number of Add, Compare and Select (ACS) operations performed [11], [21], [21]. More explicitly, the complexity of the SCL decoder [11] mostly depends on the list size L , as well as on the encoded block length N , according to $\mathcal{O}(LN \log N)$ [11]. By contrast, the complexity of the SCAN decoder depends on the maximum number I_{inner}^{\max} of internal iterations, and the encoded block length N , according to $\mathcal{O}(I_{inner}^{\max} N \log N)$ [12]. Note that, the first step in each iteration of the G-SCAN algorithm is to carry out SCL decoding, while the second step is to activate the modified-SCAN decoding [21]. Hence, the complexity of the G-SCAN algorithm depends mainly on the list size L , on the encoded block length N and on the maximum number of internal iterations I_{inner}^{\max} performed within the modified-SCAN algorithm. Hence we have, $\mathcal{O}[(I_{inner}^{\max} N \log N) + (LN \log N)]$ [21].

The complexity of the proposed hybrid decoder may be obtained by adding the complexity of the conventional SCAN algorithm and of the G-SCAN algorithm. More specifically, the complexity depends not only on the maximum number of internal iterations I_{inner}^{\max} performed by the SCAN decoder but also upon the list size L of the G-SCAN decoder. Note that, in the proposed hybrid polar decoder only $I_{inner}^{\max} = 1$ iterations are performed by the modified-SCAN algorithm within the G-SCAN decoder. Hence, the complexity of the G-SCAN polar decoder in the proposed hybrid decoder is $\mathcal{O}[(N \log N) + (LN \log N)]$.

In order to make a more detailed comparison, Table 6 compares the computational complexity of the various schemes considered in terms of the number of ACS operations performed by the various polar decoders, when adopting a polar coding rate of $R_i = 1/2$, and encoded block length of $N = 1024$, as well as various list sizes L , I_{inner}^{\max} internal iterations, and I^{\max} receiver-level iterations. Table 6 reveals that the proposed UEC-hybrid(2,L=2)-MIMO scheme imposes approximately 11% lower complexity than the JSCC benchmarker UEC-SCAN(2,2)-MIMO. This comparison is particularly relevant, since in Section VII we will show that UEC-SCAN(2,2)-MIMO is the best-performing JSCC benchmarker and it offers a similar SER performance to the proposed UEC-hybrid(2,L=2)-MIMO scheme for $I^{\max} = 4$. Furthermore, when increasing the list size from $L = 2$ to $L = 4$, the proposed UEC-hybrid(2,L=4)-MIMO offers 0.15 dB SER gain over the JSCC benchmarker UEC-SCAN(2,2)-MIMO at SER of 10^{-2} , while still having 1.8% lower complexity, as shown in Table 6. As it will be shown in Section VII, although the proposed UEC-hybrid(2,L=4)-MIMO scheme may have higher complexity than some of the benchmarkers, such

TABLE 6. Computational Complexity Analysis of Polar Decoder Algorithms in Terms of ACS Operations, as Well as the Required E_b/N_0 [dB] to Achieve a Symbol Error Rate (SER) of 10^{-3}

Benchmarkers				Proposed hybrid polar decoder			
SSCC benchmarker	I^{max}	Polar decoding complexity	required E_b/N_0 [dB]	Schemes	I^{max}	Polar decoding complexity	required E_b/N_0 [dB]
Unary-SCL(L=32)-MIMO	-	327,130	3.39	UEC-hybrid(2, L=2)-MIMO	4	584,128	1.92
Unary-SCAN(1)-MIMO	4	163,840	2.73	UEC-hybrid(2, L=4)-MIMO	4	643,616	1.85
Unary-SCAN(2)-MIMO	4	327,680	2.65	UEC-hybrid(2, L=8)-MIMO	4	762,464	1.85
Unary-G-SCAN(L=2)-MIMO	4	256,448	2.30	UEC-hybrid(2, L=4)-MIMO	1	160,904	3.94
Unary-G-SCAN(L=4)-MIMO	4	315,936	2.05	UEC-hybrid(2, L=4)-MIMO	2	321,808	2.32
Unary-G-SCAN(L=8)-MIMO	4	434,784	2.04	UEC-hybrid(2, L=4)-MIMO	3	482,712	1.95
JSCC benchmarker				UEC-hybrid(2, L=4)-MIMO	5	804,520	2.05
UEC-SCAN(1,1)-MIMO	4	327,680	2.30	UEC-hybrid(2, L=4)-MIMO	6	965,424	2.05
UEC-SCAN(1,2)-MIMO	4	491,520	2.29	UEC-hybrid(1, L=2)-MIMO	4	420,288	2.40
UEC-SCAN(2,1)-MIMO	4	491,520	2.00	UEC-hybrid(1, L=4)-MIMO	4	479,776	2.20
UEC-SCAN(2,2)-MIMO	4	655,360	1.92	UEC-hybrid(1, L=8)-MIMO	4	598,624	2.19

as UEC-SCAN(2,1)-MIMO, it is the only scheme that outperforms the best-performing SSCC benchmarker, which is the Unary-G-SCAN(L=8)-MIMO scheme of Fig. 5. In terms of the two-stage serially concatenated SSCC benchmarkers, Table 6 shows that the Unary-G-SCAN(L=2)-MIMO scheme imposes 20% lower polar decoding complexity than the Unary-SCAN(2)-MIMO benchmarker, while providing 0.3 dB gain as the analysis of Section VII will show.

VII. PERFORMANCE ANALYSIS

This section characterises the error correction and error detection performance of the proposed hybrid polar decoder in the context of our three-stage serial concatenated scheme, which we refer to as the UEC-hybrid-MIMO scheme. We compare this to the relevant JSCC and SSCC benchmarkers of Fig. 2 and Fig. 5, respectively. More specifically, we begin by characterising the proposed hybrid polar decoder in the context of the UEC-hybrid-MIMO JSCC scheme for various system parameters in Figs. 13 and 14. Then we characterise and compare the various benchmarkers that we introduced in Fig. 15. Finally, we compare the proposed hybrid polar decoder to the best of the benchmarkers in Fig. 16.

In order to characterise the performance of the various schemes, the SER plot versus the signal-to-noise ratio per bit (E_b/N_0) are recorded for the case of 2×2 Gray-mapped QPSK MIMO for transmission over an uncorrelated narrowband Rayleigh fading channel. Throughout our investigation, we adopted the polar coding rate of $R_i = 1/2$ and the encoded block length of $N = 1024$. Furthermore, the source symbol values of \mathbf{x} that obey a zeta distribution having a parameter value of $p_1 = 0.797$, are adopted as [22]. Note that all benchmarkers considered have the same DCMC capacity bound of -2.26 dB, since they all have the same effective throughput of $\eta = 1.5236$, as detailed in Section III-A.

Fig. 13 illustrates the beneficial impact of increasing the numbers of receiver-level iterations $I^{max} = \{1, 2, 3, 4, 5, 6\}$,

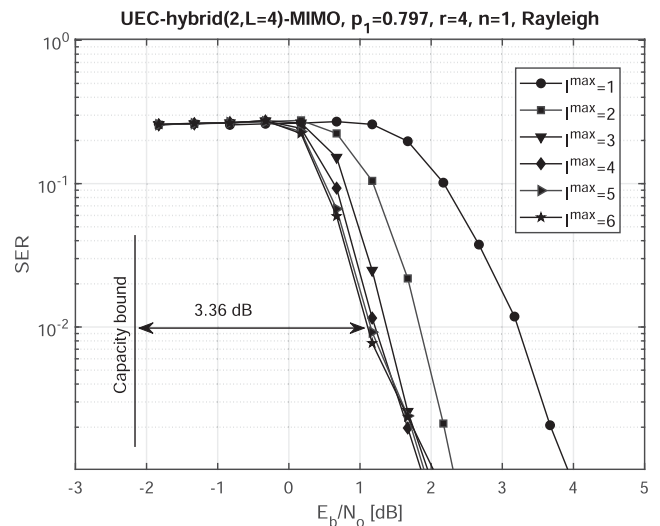


FIGURE 13. SER performance of the proposed UEC-hybrid(2,L=4)-MIMO scheme when using various numbers of receiver-level iterations $I^{max} = \{1, 2, 3, 4, 5, 6\}$ in the context of three-stage concatenated JSCC scheme, where the source is zeta distributed with the parameter $p_1 = 0.797$, and $I^{max}_{inner} = 2$ internal iterations within the SCAN decoder and the list size $L = 4$ adopted in the G-SCAN decoder of the hybrid polar decoder, when communicating over an uncorrelated narrowband Rayleigh fading channel.

when the proposed hybrid polar decoder is applied in the three-stage concatenated JSCC scheme of Fig. 2. More specifically, the proposed hybrid polar decoder adopted $I^{max}_{inner} = 2$ within the upper SCAN decoder, as well as the list size of $L = 4$ within the lower G-SCAN polar decoder. As expected, during the successive iterations between the outer UEC decoder, hybrid polar decoder, and the inner MIMO detector, the soft-decision estimates of the transmitted symbols become more accurate as and when more extrinsic information is iteratively exchanged. Fig. 13 shows that increasing the number of receiver-level iterations I^{max} performed by the proposed JSCC

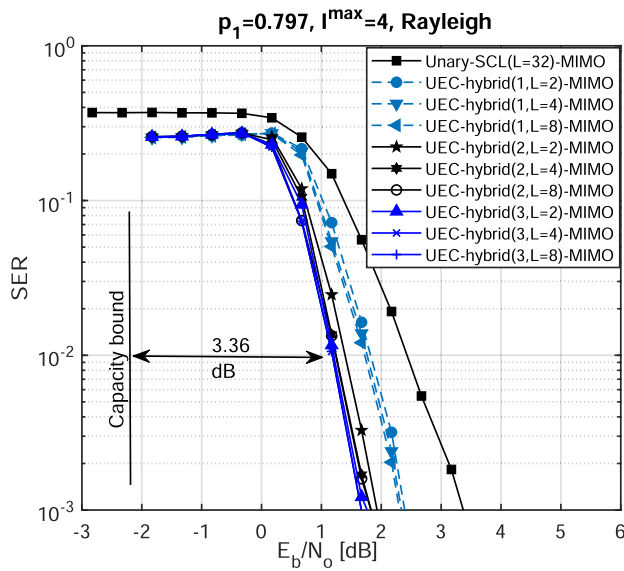


FIGURE 14. SER performance of the proposed UEC-hybrid-MIMO scheme, when adopting the various number of inner iterations I_{inner}^{max} , as well as list sizes L , for the case of the source is zeta distributed with the parameter $p_1 = 0.797$, and $I_{inner}^{max} = 4$ receiver-level iterations, when communicating over an uncorrelated narrowband Rayleigh fading channel.

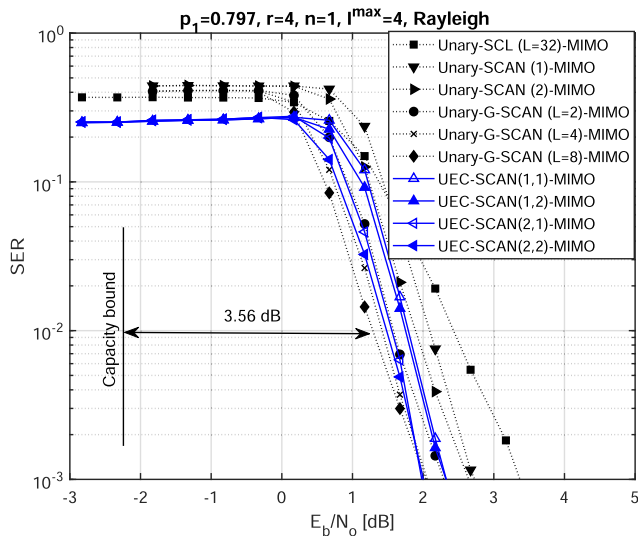


FIGURE 15. SER performance of various SSCC and JSSC benchmarks, where the source is zeta distributed with the parameter $p_1 = 0.797$, when communicating over an uncorrelated narrowband Rayleigh fading channel.

UEC-hybrid-MIMO scheme improves the performance, owing to the iterative feedback gain offered by not only the inner 2×2 QPSK detector, but also by the outer UEC decoder. For example, increasing the number of receiver-level iterations from $I_{inner}^{max} = 1$ to $I_{inner}^{max} = 2$ provides more than 1.5 dB gain. However, it may also be observed that the performance improvements gradually saturate, as the number of receiver-level iterations is increased. For example, increasing the number of receiver-level iterations from $I_{inner}^{max} = 3$ to $I_{inner}^{max} = 4$ provides only 0.2 dB gain. Hence, as mentioned in Section VI, $I_{inner}^{max} = 4$ may be recommended for striking an attractive performance

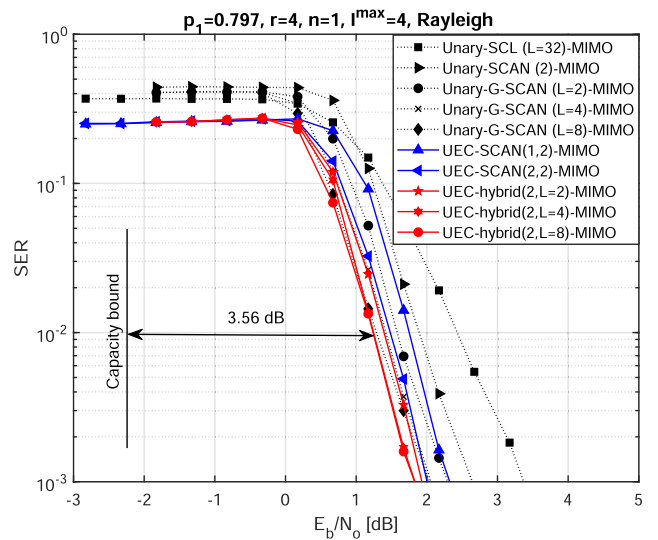


FIGURE 16. SER performance of the proposed UEC-hybrid-MIMO scheme and various benchmarks, when adopting various list sizes L , for the case of the source is zeta distributed with the parameter $p_1 = 0.797$, and $I_{inner}^{max} = 5$ receiver-level iterations are applied when communicating over an uncorrelated narrowband Rayleigh fading channel.

vs. complexity trade-off for the proposed UEC-hybrid-MIMO scheme.

Fig. 14 illustrates the impact of adopting various numbers of inner iterations I_{inner}^{max} within the upper SCAN decoder, as well as various list sizes L for the lower G-SCAN polar decoder, when the proposed hybrid polar decoder is applied in the three-stage concatenated JSSC UEC-hybrid-MIMO scheme of Fig. 2. As may be expected, increasing the number of inner iterations I_{inner}^{max} of the upper SCAN decoder improves the performance. For example, increasing $I_{inner}^{max} = 1$ to $I_{inner}^{max} = 2$ provides 0.4 dB gain, when a constant list size of $L = 2$ is used by the lower G-SCAN decoder. However, further increasing the number of inner iterations from $I_{inner}^{max} = 2$ to $I_{inner}^{max} = 3$ provides only 0.2 dB gain. Hence, as mentioned in Section VI, $I_{inner}^{max} = 2$ may be recommended for striking an attractive trade-off between the performance and the complexity of the proposed hybrid polar decoder.

Similarly, when a constant number of inner iterations I_{inner}^{max} is used for the upper SCAN decoder, increasing the list size used in the lower G-SCAN decoder improves the performance. For example, increasing the list size from $L = 2$ to $L = 4$ provides 0.15 dB gain, when a constant list size of $I_{inner}^{max} = 2$ is used by the upper SCAN decoder. However, it may also be observed that the performance improvements saturate, as the list size is further increased. For example, increasing the list size from $L = 4$ to $L = 8$ does not provide any significant performance gain, despite increasing the complexity by about 15%. Hence, as mentioned in Section VI, a list size of $L = 4$ may be recommended for striking an attractive trade-off between the performance and complexity of the proposed hybrid polar decoder.

The two-stage concatenated SSCC benchmark schemes of Section IV are characterized in Fig. 15 for various polar

decoders. More specifically, the Unary-SCAN-MIMO benchmark of Fig. 5 employs a SISO SCAN polar decoder, the Unary-G-SCAN-MIMO benchmark of Fig. 5 uses a SISO G-SCAN polar decoder, while the Unary-SCL-MIMO benchmark of Fig. 6 relies on a hard-decision SCL decoder. As mentioned in Section VI, while the SCAN and G-SCAN decoders carry out I^{\max} iterations with the MIMO detector, the SCL decoder is unable to iteratively exchange extrinsic information with either an outer or an inner decoder. Hence, in this scenario, the Unary-SCL-MIMO benchmark of Fig. 6 can only benefit from one-shot MIMO detection, polar decoding, and source decoding. Fig. 15 shows that the Unary-SCAN(1)-MIMO benchmark of Fig. 5 provides 0.3 dB gain by using $I^{\max} = 4$ receiver-level iterations at a SER of 10^{-2} , when compared to the Unary-SCL(L=32)-MIMO benchmark of Fig. 6. Additionally, Fig. 15 shows that increasing the number of internal iterations I_{inner}^{\max} of the SCAN decoder in the Unary-SCAN-MIMO benchmark provides only limited gain, despite increasing the polar decoding complexity. For example, increasing the number of internal iterations from $I_{inner}^{\max} = 1$ to $I_{inner}^{\max} = 2$ provides only 0.2 dB gain at the cost of doubling the polar decoding complexity, as mentioned in Section VI. Furthermore, Fig. 15 also shows that the Unary-G-SCAN-MIMO benchmark of Fig. 5 outperforms all other SSCC benchmarkers. For example, the Unary-G-SCAN(L=2)-MIMO scheme provides 0.8 dB gain over the Unary-SCL(L=32)-MIMO benchmark, as seen in Fig. 15. Additionally, Fig. 15 demonstrates that the Unary-G-SCAN(L=2)-MIMO benchmark provides 0.3 dB gain over the Unary-SCAN(2)-MIMO benchmark, while requiring 20% lower polar decoding complexity, as mentioned in Section VI. Clearly, the Unary-G-SCAN(L=8)-MIMO benchmark is the best-performing SSCC benchmark, which is capable of operating within 3.56 dB of the DCMC capacity bound at an SER of 10^{-2} .

On the other hand, the three-stage concatenated JSCC UEC-SCAN-MIMO benchmark of Fig. 2 is also characterised in Fig. 15. Here, the fixed decoder activation order of {MIMO, upper SCAN polar decoder, UEC, lower SCAN polar decoder} is employed until the maximum number of receiver-level iterations I^{\max} is reached. As shown in Fig. 15, the UEC-SCAN(2,1)-MIMO benchmark offers superior performance compared to the UEC-SCAN(1,2)-MIMO benchmark by providing 0.25 dB gain. This shows that the iterations performed by the upper SCAN decoder are more beneficial than those of the lower SCAN decoder. This may be explained by the higher mutual information that the SCAN decoder generates for its decoded extrinsic LLR vector $\tilde{\mathbf{u}}_e$ relative to that generated for the encoded extrinsic LLR $\tilde{\mathbf{d}}_e$. Additionally, Fig. 15 reveals that the JSCC UEC-SCAN-MIMO benchmark of Fig. 2 may outperform the SSCC Unary-SCAN-MIMO benchmark. For example, Fig. 15 shows that the JSCC benchmark UEC-SCAN(2,2)-MIMO provides 0.40 dB gain over the SSCC benchmark Unary-SCAN(2)-MIMO, when they both employ $I^{\max} = 4$ receiver-level iterations. This reveals that increasing the

maximum number of internal iterations only provides limited gain, even when the SCAN decoder exchanges extrinsic information with an inner decoder, such as the 2×2 QPSK MIMO detector. On the other hand, when the SCAN decoder is concatenated with both an inner and an outer decoder, higher gains may be achieved, since extrinsic information is beneficially exchanged amongst three concatenated decoders. However, although the SCAN decoder is iterated with both an inner and the outer decoder in the UEC-SCAN(2,2)-MIMO benchmark, it is still unable to outperform the best SSCC benchmark, namely the Unary-G-SCAN(L=8)-MIMO.

Fig. 16 compares the SER performance of the proposed hybrid polar decoder to that of the above-mentioned JSCC and SSCC benchmarkers, while considering different list sizes L , but a constant number of inner iteration, namely $I_{inner}^{\max} = 2$. As shown in Fig. 16, the proposed hybrid polar decoder is the only one that is able to outperform the best SSCC benchmark, which is the Unary-G-SCAN(L=8)-MIMO. More specifically, the proposed JSCC UEC-hybrid(2,L=4)-MIMO scheme provides 0.2 dB gain over the SSCC benchmarker Unary-G-SCAN(L=8)-MIMO at SER of 10^{-3} . In comparison to a three-stage serial concatenated JSCC benchmark, the proposed SISO UEC-hybrid(2,L=2)-MIMO scheme offers approximately 11% complexity reduction over the UEC-SCAN(2,2)-MIMO benchmark, while achieving similar SER performance. Additionally, the proposed UEC-hybrid(2,L=2)-MIMO scheme achieves a 0.75 dB SNR gain, over the two-stage serial concatenated SSCC Unary-SCAN(2)-MIMO benchmark.

VIII. SUMMARY AND CONCLUSION

Prior to this article, SISO polar decoders have not been characterized in a holistic MIMO transceiver context in a three-stage concatenated turbo architecture along with an inner and an outer decoder. Motivated by filling this knowledge gap, we have proposed a novel hybrid polar decoder capable of accepting *a-priori* LLRs pertaining to both the decoded and encoded bits, and producing extrinsic LLRs pertaining to both the decoded and encoded bits in return. More specifically, we proposed a hybrid polar decoder that inherits the error correction performance benefits of the SCL polar decoder, as well as the soft decision benefit of the SCAN decoder. To elaborate further, we adopted a SCAN decoder for processing the LLRs provided by the concatenated outer decoder and the G-SCAN decoder for processing the LLRs provided by the concatenated inner decoder. Furthermore, we presented the 3D EXIT chart analysis of our turbo-MIMO transceiver in order to characterise the iterative exchange of extrinsic information amongst the three concatenated codes leading to iterative detection convergence.

Our simulation results demonstrated that the proposed three-stage serially concatenated JSCC UEC-hybrid(2,L=2)-MIMO scheme is capable of outperforming the SSCC Unary-SCAN(2)-MIMO benchmark by offering 0.75 dB gain. Furthermore, the proposed UEC-hybrid(2,L=2)-MIMO scheme imposes approximately 11% lower complexity than

the best-performing JSCC UEC-SCAN(2,2)-MIMO benchmark, when both schemes operate at a similar SER. Furthermore, increasing the SCL list size from $L = 2$ to $L = 4$ enables the proposed UEC-hybrid(2,L=4)-MIMO scheme to achieve 0.25 dB gain over the UEC-SCAN(2,2)-MIMO benchmark, while improving 1.8% lower complexity. Our future work may consider different combinations of upper and lower polar decoders within the framework of the proposed hybrid polar decoder. Furthermore, other applications of polar codes in three-stage concatenated iterative receivers may also be considered. Finally, near-capacity irregular polar coding schemes may be designed by relying on the principles detailed in [36].

REFERENCES

- [1] 3rd Generation Partnership Project (3GPP), "NR; Multiplexing and channel coding," 3GPP, Sophia Antipolis, France, Tech. Specification, TS 38.212 (Release 15) V15.6.0, Jun. 2019.
- [2] D. Na, W.-G. Seo, H. Shim, K. Ryu, and K. Choi, "A very fast joint detection for polar-coded SCMA," *IEEE Access*, vol. 10, pp. 38534–38544, 2022.
- [3] X. Wu, Y. Wang, and C. Li, "Low-complexity CRC aided joint iterative detection and SCL decoding receiver of polar coded SCMA system," *IEEE Access*, vol. 8, pp. 220108–220120, 2020.
- [4] Z. Pan, E. Li, L. Zhang, J. Lei, and C. Tang, "Design and optimization of joint iterative detection and decoding receiver for uplink polar coded SCMA system," *IEEE Access*, vol. 6, pp. 52014–52026, 2018.
- [5] L. Xiang, Y. Liu, C. Xu, R. G. Maunder, L.-L. Yang, and L. Hanzo, "Iterative receiver design for polar-coded SCMA systems," *IEEE Trans. Commun.*, vol. 69, no. 7, pp. 4235–4246, Jul. 2021.
- [6] X. Deng et al., "Joint detection and decoding of polar-coded OFDM-IDMA systems," *IEEE Trans. Circuits Syst. I: Regular Papers*, vol. 66, no. 10, pp. 4005–4017, Oct. 2019.
- [7] T. Xie, Y. Y. Tai, and J. Zhu, "Polar codes for NAND-based SSD systems: A joint source channel coding perspective," in *Proc. IEEE Inf. Theory Workshop*, 2017, pp. 196–200.
- [8] Y. Dong, K. Niu, J. Dai, S. Wang, and Y. Yuan, "Joint source and channel coding using double polar codes," *IEEE Commun. Lett.*, vol. 25, no. 9, pp. 2810–2814, Sep. 2021.
- [9] Y. Dong, K. Niu, J. Dai, and S. Wang, and Y. Yuan, "Joint successive cancellation list decoding for the double polar codes," *IEEE Commun. Lett.*, vol. 26, no. 8, pp. 1715–1719, Aug. 2022.
- [10] E. Arıkan, "A performance comparison of polar codes and reed-muller codes," *IEEE Commun. Lett.*, vol. 12, no. 6, pp. 447–449, Jun. 2008.
- [11] I. Tal and A. Vardy, "List decoding of polar codes," *IEEE Trans. Inf. Theory*, vol. 61, no. 5, pp. 2213–2226, May 2015.
- [12] U. U. Fayyaz and J. R. Barry, "A low-complexity soft-output decoder for polar codes," in *Proc. GLOBECOM - IEEE Glob. Telecommun. Conf.*, 2013, vol. 2, pp. 2692–2697.
- [13] E. Arıkan, "Channel polarization: A method for constructing capacity-achieving codes for symmetric binary-input memoryless channels," *IEEE Trans. Inf. Theory*, vol. 55, no. 7, pp. 3051–3073, Jul. 2009.
- [14] Y. Zhang, Q. Zhang, X. Pan, Z. Ye, and C. Gong, "A simplified belief propagation decoder for polar codes," in *Proc. IEEE Int. Wireless Symp.*, 2014, pp. 1–4.
- [15] L. Hanzo, T. H. Liew, and B. L. Yeap, *Turbo Coding, Turbo Equalisation and Space-Time Coding*. New York, NY, USA: Wiley, 2002.
- [16] J. P. Woodard and L. Hanzo, "Comparative study of turbo decoding techniques: An overview," *IEEE Trans. Veh. Technol.*, vol. 49, no. 6, pp. 2208–2233, Nov. 2000.
- [17] L. Hanzo, J. P. Woodard, and P. Robertson, "Turbo decoding and detection for wireless applications," *Proc. IEEE*, vol. 95, no. 6, pp. 1178–1200, Jun. 2007.
- [18] C. Douillard et al., "Iterative correction of intersymbol interference: Turbo-equalization," *Eur. Trans. Telecommun.*, vol. 6, no. 5, pp. 507–511, 1995.
- [19] C. S. Park, Y. P. E. Wang, G. Jöngren, and D. Hammarwall, "Evolution of uplink MIMO for LTE-advanced," *IEEE Commun. Mag.*, vol. 49, no. 2, pp. 112–121, Feb. 2011.
- [20] M. Tüchler and A. C. Singer, "Turbo equalization: An overview," *IEEE Trans. Inf. Theory*, vol. 57, no. 2, pp. 920–952, Feb. 2011.
- [21] Z. B. K. Egilmez, L. Xiang, R. G. Maunder, and L. Hanzo, "A soft-input soft-output polar decoding algorithm for turbo-detection in MIMO-aided 5G new radio," *IEEE Trans. Veh. Technol.*, vol. 71, no. 6, pp. 6454–6468, Jun. 2022.
- [22] W. Zhang, Y. Jia, X. Meng, M. F. Breyza, R. G. Maunder, and L. Hanzo, "Adaptive iterative decoding for expediting the convergence of unary error correction codes," *IEEE Trans. Veh. Technol.*, vol. 64, no. 2, pp. 621–635, Feb. 2015.
- [23] K. Lakovic, T. Tian, and J. Villasenor, "Iterative decoder design for joint source-channel LDPC coding," in *Proc. IEEE EUROCON Int. Conf. Comput. Tool*, 2005, pp. 486–489.
- [24] R. G. Maunder, W. Zhang, T. Wang, and L. Hanzo, "A unary error correction code for the near-capacity joint source and channel coding of symbol values from an infinite set," *IEEE Trans. Commun.*, vol. 61, no. 5, pp. 1977–1987, May 2013.
- [25] A. Zribi, R. Pyndiah, S. Zaibi, F. Guilloud, and A. Bouallegue, "Low-complexity soft decoding of Huffman codes and iterative joint source channel decoding," *IEEE Trans. Commun.*, vol. 60, no. 6, pp. 1669–1679, Jun. 2012.
- [26] A. Elkelesh, M. Ebada, S. Cammerer, and S. T. Brink, "Belief propagation list decoding of polar codes," *IEEE Commun. Lett.*, vol. 22, no. 8, pp. 1536–1539, Aug. 2018.
- [27] M. Geiselhart, A. Elkelesh, M. Ebada, S. Cammerer, and S. T. Brink, "CRC-aided belief propagation list decoding of polar codes," in *Proc. IEEE Int. Symp. Inf. Theory*, Los Angeles, CA, USA, 2020, pp. 395–400, doi: [10.1109/ISIT44484.2020.9174249](https://doi.org/10.1109/ISIT44484.2020.9174249).
- [28] M. El-Hajjar and L. Hanzo, "Multifunctional MIMO systems: A combined diversity and multiplexing design perspective," *IEEE Wireless Commun.*, vol. 17, no. 2, pp. 73–79, Apr. 2010.
- [29] M. F. Breyza et al., "Exponential Golomb and rice error correction codes for generalized near-capacity joint source and channel coding," *IEEE Access*, vol. 4, pp. 7154–7175, 2016.
- [30] H. V. Nguyen, C. Xu, S. X. Ng, and L. Hanzo, "Near-capacity wireless system design principles," *IEEE Commun. Surv. Tut.*, vol. 17, no. 4, pp. 1806–1833, Fourthquarter 2015.
- [31] W. Zhang, R. G. Maunder, and L. Hanzo, "On the complexity of unary error correction codes for the near-capacity transmission of symbol values from an infinite set," in *Proc. IEEE Wireless Commun. Netw. Conf.*, 2013, pp. 2795–2800.
- [32] S. ten Brink and B. M. Hochwald, "Detection thresholds of iterative MIMO processing," in *Proc. IEEE Int. Symp. Inform. Theory*, Lausanne, Switzerland, 2002, p. 22, doi: [10.1109/ISIT.2002.1023294](https://doi.org/10.1109/ISIT.2002.1023294).
- [33] M. El-Hajjar and L. Hanzo, "EXIT charts for system design and analysis," *IEEE Commun. Surv. Tut.*, vol. 16, no. 1, pp. 127–153, First Quarter 2014.
- [34] J. Sayir, "EXIT chart approximations using the role model approach," in *Proc. IEEE Int. Symp. Inf. Theory*, 2010, pp. 694–698, doi: [10.1109/ISIT.2010.5513589](https://doi.org/10.1109/ISIT.2010.5513589).
- [35] J.-S. Kim, S.-H. Moon, and I. Lee, "A new reduced complexity ML detection scheme for MIMO systems," *IEEE Trans. Commun.*, vol. 58, no. 4, pp. 1302–1310, Apr. 2010.
- [36] L. Hanzo, R. G. Maunder, and J. Wang, *Near-Capacity Variable Length Coding: Regular and EXIT-Chart Aided Irregular Designs*. New York, NY, USA: Wiley, 2011.



ZEYNEP B. KAYKAC EGILMEZ (Member, IEEE) received the dual B.Eng. (Hons.) degrees in electrical and electronic engineering and in industrial engineering from Kirikkale University, Kirikkale, Türkiye, in 2014, and the M.Sc. and Ph.D. degrees from the Next Generation Wireless Group, School of Electronics and Computer Science (ECS), University of Southampton, Southampton, U.K., in 2017 and in 2020, respectively. She is currently a Postdoctoral Research Fellow of underwater communication and networking, University of Southampton. Her research interests include channel coding, especially polar coding in wireless communication, and waveform design for underwater communication channels.



ROBERT G. MAUNDER (Senior Member, IEEE) received the B.Eng. (first-class Hons.) degree in electronic engineering and the Ph.D. degree in telecommunications from the School of Electronics and Computer Science, University of Southampton, Southampton, U.K., in 2003 and 2007, respectively. He began a lectureship in 2007 and was promoted to Associate Professor in 2013 and to Professor in 2017. He has authored or coauthored a number of IEEE papers in these areas. He is the Founder and CTO of AccelerComm Ltd.,

which is commercialising his research as soft-IP. His research interests include joint source/channel coding and the holistic design of algorithms and hardware implementations for wireless communications. He was awarded Senior Member status of IEEE in 2012, Chartered Engineer status of the IET in 2013, and Fellow status of the IET in 2017.



MOHAMMED EL-HAJJAR (Senior Member, IEEE) received the Ph.D. degree in wireless communications from the University of Southampton, Southampton, U.K., in 2008. Following the Ph.D., he joined Imagination Technologies as a Design Engineer. Since 2012, he has been with the School of Electronics and Computer Science, University of Southampton, where he is currently a Professor. He has authored or coauthored a Wiley-IEEE book and in excess of 100 journal and conference papers in addition to many patents. His research

interests include the development of intelligent communications systems, energy-efficient transceiver design, millimeter wave communications, machine learning for wireless communications, radio over fiber network design and underwater communications. He was the recipient of several academic awards



LAJOS HANZO (Life Fellow, IEEE) received the master's and Doctorate degrees from the Technical University (TU) of Budapest, Budapest, Hungary, in 1976 and 1983, respectively, the Doctor of Science (D.Sc.) degree from the University of Southampton, Southampton, U.K., in 2004, and the joint Honorary Doctorate degree from the TU of Budapest in 2009 and The University of Edinburgh, Edinburgh, U.K., in 2015. He is currently a Foreign Member of the Hungarian Academy of Sciences and the Former Editor-in-Chief of the

IEEE Press. He has authored or coauthored more than 2000 contributions at IEEE Xplore, 19 Wiley-IEEE Press books, and has helped the fast-track career of 123 Ph.D. students. More than 40 of them are Professors at various stages of their careers in academia and many of them are leading scientists in the wireless industry. He has served several terms as a Governor of IEEE ComSoc and VTS. He is also a Fellow of the Royal Academy of Engineering (FREng), the IET, and EURASIP. He was the recipient of the 2022 Eric Summer Field Award.